Journal of
Computational and Theoretical Nanoscience
Vol. 5, 862–893, 2008

High-Temperature Photonic Structures. Thermal Barrier Coatings, Infrared Sources and Other Applications

Valery Shklover[1,*], Leonid Braginsky[1], Gregoire Witz[1], Matthew Mishrikey[2], and Christian Hafner[2]

[1] *Laboratory of Crystallography, Department of Materials, ETH Zürich, 8093 Zürich, Switzerland*
[2] *Laboratory of Electromagnetic Fields and Microwave Electronics, ETH Zürich, 8092 Zürich, Switzerland*

Successful high-temperature photonic structure design requires a thorough theoretical understanding in several disciplines. In this review, we examine many theoretical questions, as well as published examples of these structures. Research on this topic started with studies of Bragg mirrors, and progressed rapidly as a result of developments in the field of photonic crystals. The practical applications, which have benefited most from this research, have been ceramic thermal barrier coatings for gas turbines, and selective emitters for thermophotovoltaic applications. Materials and fabrication research has allowed for the construction of one-, two- and three-dimensional structures which can operate under extreme temperatures in excess of 1000 °C. Boundary condition approaches can be used to extract the transmission spectra of regular and irregular photonic structures. In particular, it is possible to estimate the propagation of waves in unorganized granular materials and in materials with large pores, where the average size exceeds the mean photon wavelength. Further, we examine the relationship between structure disorder, photon mean free path, and radiation heat transfer. Finally, we outline various numerical techniques used for solving photonic structures, including time and frequency domain techniques, discretization methods, and semi-empirical approaches. By means of an example, we discuss practical steps helpful for the optimization of such structures. A design example for high-temperature photonic structure with low layer count is presented.

Keywords: Photonics, High-Temperature Materials, Thermal Barrier Coatings, Thermophotovoltaics, IR Sources.

CONTENTS

1. INTRODUCTION

With the recent success in development of photonic crystals or photonic band gap materials (PBGM) (see for example[1]), it has been shown that modulated structures can be used to efficiently control electromagnetic waves emitted by high-temperature sources and in high temperature environments. These High-Temperature Photonic Structures (HTPS) are analogous to "normal" photonic crystals, and can be designed for different photonic functions, such as reflection, filtering, and selective absorption.

---

[*] Author to whom correspondence should be addressed.

1546-1955/2008/5/862/032 doi:10.1166/jctn.2008.003

HTPS are further required to have a bandgaps in the infrared regime, while operating at temperatures up to 1000 °C or higher. HTPS may not exhibit significant phase, chemistry or microstructure changes under prolonged exposure at high temperatures as shown in Figure 2.

Multilayer refractory metal oxide stacks, built out of alternating layers of high and low refraction index materials, constitute the simplest one dimensional HTPS. The layer thicknesses and index contrasts of the metal oxide stacks can be used to reflect radiated energy of

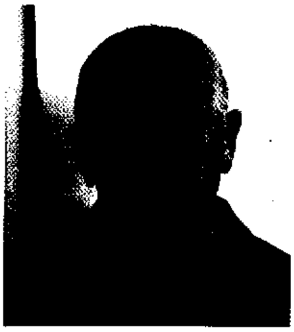

Valery Shklover completed both undergraduate and graduate studies in engineering of materials for electronics at Moscow Institute of Fine Chemical Technology in 1971. He earned his Ph.D. (in Russia candidate) in physical chemistry from Nesmeyanov-Institute of Organo-Element Compounds of the Russian Academy of Sciences in 1974 and made his second dissertation (in Russia doctor) in 1981. Under his supervision, six dissertations were prepared. Since 1989 he is working in Switzerland, first at the University of Bern, than at University of Zürich, and since 1991 he is senior scientist at the Laboratory of Crystallography of the Department of Materials of the ETH Zurich. Between 1991 and 1995 V. Shklover was working at the ETH on energy harvesting and storage projects for the Swiss Office of Energy. His main scientific interests are solid-state chemistry, nanostructures, photonics, hybrid organic–inorganic structures, and protection coatings. He is author of more than 120 peer-reviewed publications in Russian and in international journals. He is manager of several industry-oriented projects in the field of nanostructures, protection coatings, sensors. Currently, he owns 5 patents.

Leonid Braginsky was born in Frunze (Kyrgyzstan) in 1956. He received his M.S. degree in theoretical physics from Kyrgyz State University in 1978, and a Ph.D. degree in condensed matter physics from the Institute of Semiconductor Physics (Novosibirsk) in 1999. He is a Senior Researcher at the Institute of Semiconductor Physics and Assistant Professor at the Novosibirsk State University. His research interests include condensed matter theory, electronic and optical properties of low dimensional systems: microstructures, superlattices, nanostructures, quantum dots, and photonic crystals; physical phenomena on an interface, transport and optical phenomena.

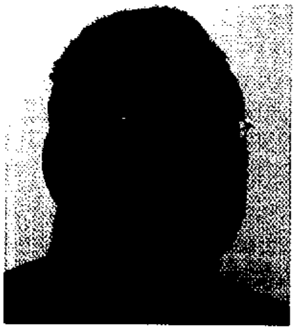

Grégoire Witz obtained a M.Sc. in Physics of Condensed Matter at the University of Geneva in 1998 and Ph.D. in Applied Physics on the preparation and characterization of Bi,Pb(2223) based superconductors having reduced AC losses at the University of Geneva in 2003. He worked from 2003 to 2005 as a research associate in the group of Applied Physics at University of Geneva on the characterization and simulation of the erosion process in electron discharge machining. He was from 2005 to 2007 a research associate in the Department of Crystallography at ETH Zürich, working on the high temperature stability, decomposition mechanisms and hot corrosion of ytrria stabilized zirconia thermal barrier coatings. He is currently working at ALSTOM (Schweiz) AG in the Department of Turbine Transverse Technologies where is responsible of the characterization and development of thermal barrier coatings.

Matthew Mishrikey graduated with B.S. (2002), and M.Eng. (2005) degrees in electrical engineering and computer science from the Massachusetts Institute of Technology. His graduate coursework was in control theory, electromagnetics, and electro-hydrodynamics. For his master's degree, he developed a system for the detection and mitigation of electrical arcing in automotive wiring harnesses. He worked as a research engineer at the BMW Group headquarters in Munich, Germany, where he worked on recuperative energy systems and prototype vehicles with electrical starter-generators. Matthew is currently a doctoral student at the Laboratory for Electromagnetic Fields and Microwave Electronics. His current research is in the field of metamaterials for microwave shielding as well as for optical applications. His work focuses on numerical techniques for analysing, designing, and optimizing photonic structures. He helps teach basic courses in antenna theory and fundamental electromagnetics.

Christian V. Hafner was born in Zurich, Switzerland, in 1952. He received his diploma and Ph.D. degree in electrical engineering from the ETH Zurich, in 1975 and 1980 respectively. In 1987 he got his venia legendi for analytical and numerical calculations of electromagnetic fields from the ETH Zurich. In 1999 he was given the title of Professor. He currently is the head of the Computational Optics Group (COG) at the IFH, ETH Zurich. Since 1976 he was a scientific assistant and lecturer at the ETH Zurich, where he studied different topics of electricity and magnetism. Since 1980 he developed the MMP code for numerical computations of dynamic fields for a large range of applications (electrostatics, guided waves on different structures, scattering, EMC). In addition he works on philosophical and historical concepts of physics and engineering, evolutionary and genetic strategies for optimization, computer graphics and animation, and on 'strange' theories (Chaos theory, fractals in classical electromagnetics, cellular automata for electromagnetics, irregular grid worlds, etc.).

a required wavelength range, prescribed by the temperature of the external radiation source. The two main applications of one dimensional HTPS are thermal barrier coatings (TBC), used for the transfer of fuel energy into electricity, and thermophotovoltaics (TPV), used for the transfer of thermal energy into electricity. It was demonstrated that periodicity of silicon based HTPS can be used to control emission spectra for TPV.

As an example of three-dimensional HTPS, silicon emitters of IR radiation were studied after initial work on photonic crystals by Yablonovich[2] and John.[3] In the following years, efforts were undertaken to design high power emitters of narrowband IR radiation corresponding to the absorption band of photovoltaic (PV) diodes. These structures were initially fabricated from refractory metals to remain stable at high temperatures in vacuum.[4] Refractory metal designs did not have the main drawback of earlier rare earth selective emitters, which had uncontrollable high emission spectral bands.[5]

One focus of this review is on the mechanism of photon heat transfer. There is an ecology motivated trend towards higher operation temperatures in order to increase the efficiency of gas turbines. Though some important applications such as thermal barrier coatings require a consideration of other mechanisms of heat transfer, there are many good reviews devoted to phonon thermal conductivity. High temperature conditions imply significant radiation heat transfer (Radiation Thermally Protective Coatings, RTBC). According to some estimates, the increase of the radiation reflectance by means of nanolayered coatings, provided they do not exhibit significant sintering, may decrease the surface temperature of gas turbine blades by up to 180 °C, which could lead to a significant improvement of blade lifetime.[6] The need for highly structured protection coatings to reduce radiation heat transfer and for use in optical sensors for non-intrusive monitoring has been discussed.[7]

An efficient RTBC must possess the properties of a good omnidirectional reflector (ODR). A good ODR is a coating with high reflection ($R \geq 99.5\%$) for all angles of incidence for both polarizations over a wide spectral range.[8,9]

There are different approaches for reducing radiative heat transfer.[7] There are no known reflective layers capable of withstanding long-term erosion conditions on gas turbine blades. Direct introduction of IR absorbers into oxide protection coatings can lead to an increase of phonon thermal conductivity. The fabrication of multilayer photonic coatings can meet significant technological problems in providing high-quality interface structures on protection coatings, in order to achieve significant reflectivity.

This review starts with a characterization of the requirements of stable materials and structures, capable of withstanding high temperature environments. In the extreme, we consider environments in excess of 1000 °C, but we also consider some structures designed for the significantly lower temperatures around 400 °C, in particular well studied silicon based structures.

We consider expressions of radiative heat conductivity, the temperature dependence of photon mean free path, and the influence and monitoring of photonic structure imperfections such as nano- and microporosity. Several published HTPS are described with a short description of the fabrication methods in each figure caption. Methods for simulating photonic structures with corresponding examples are also discussed.

2. MATERIAL SCIENCE ASPECT OF HIGH TEMPERATURE PHOTONIC STRUCTURES

High temperature stability is unquestionably the most critical issue of photonic structure design. This means that not only refraction index, modulation periods and other optical properties, but also melting point, thermal stability, oxidation stability and mechanical properties become critical parameters (see Table I). Any HTPS has to be designed as a part of a complex system where the interactions between all components must be taken into account to ensure that the system will be able to run smoothly during its entire lifetime.

HTPS constituents must withstand stresses arising from maximum operating temperature, number of cycles, heating and cooling rates, temperature gradients, and

Table I. Physical properties of some mentioned in this review materials (T_m is melting point, γ is density, κ is thermal conductivity at 300 K, α is coefficient of thermal expansion at 300 K, n is refraction index).

Material	n	T_m, °C	ρ, g cm^{-3}	κ, W m^{-1}K^{-1}	α, m^{-1} K^{-}
Al_2O_3	1.60, 1.76 (at 1 μm)[99]	2050	3.98	33	4.6
CeO_2	2.3 at 800 nm	2100	7.65	2.93	8
HfO_2	1.98	2900	10.2	1.95	6.5
SiO_2	1.95, 1.45 (at 1 μm)[100]	1600	2.20	1.36	0.6
ZrO_2	2.10	2715	5.89	3	10.3
Y_2O_3	1.9 (at 1 μm)[101]	2390	5.01	8	7.5
YSZ	2.12 (at 1 μm)[102]	2715	6.05	2	10.6
MgO	1.72 (at 1 μm)[103]	2800	3.58	40–50	9.8
YAG–YIG	2.20 ($x = 0$ at 1 μm)[104]	1970	4.5–4.6	~5[105]	9.1
$Y_3Al_xFe_{5-x}O_{12}$	1.81 ($x = 5$ at $\lambda = \infty$)[106]				
$La_{1-x}Nd_xMgAl_{11}O_{19}$	1.77 (at $\lambda = \infty$)[107]	>1850	4.03	1.7[108]	10.1[108]
Mullite, $3Al_2O_3 \cdot 2SiO_2$	1.64	1810	3.05	6	5.4
W	3.00 (at 1 μm)[109]	3422	19.25	173	4.5
Si	3.35 3.62 (at 1 μm)[110]	1414	2.33	149	2.6
Ti	3.35 (at 1 μm)[111]	1670	4.61	22	8.6
SiC	2.55	2830	3.1	3.7	4.3
Graphite	2.77 (at 700 nm)[112]	*	2.16	160	7.8

*For graphite T (glass point) > 1800 K, T (decomposition temperature) 3900–4000 K.

mechanical loads. To give an example of what could be the current requirements for HTPS, the following figures could be taken from the state of the art gas turbine industry. Gas temperature in a combustor may run between 1700 and 2000 Kelvin,[10] the radiant flux from gas and soot is around 230 000 W m^{-2} correspond to a blackbody temperature of 1419 K.[11] Next generation TBC materials are expected to operate at surface temperatures as high as 1900 K.[6] The failure requirements of TBC materials are formulated as compliance to withstand strains due to thermal expansion mismatch between ceramic coatings and underlying metal alloys, thermodynamic compatibility between TBC and TGO, and "prime reliant" properties.[7]

The design of the whole system (Fig. 1) should allow that:

(1) the HTPS itself is able to resist high temperatures during the entire system operating life without having a significant alteration of its photonic properties;

(2) the hot gas environment will not degrade the photonic structure material and its photonic properties;

(3) there is no reaction between the photonic structure and the underlying materials that can lead to failure of one of the constituents or to a degradation of the photonic properties. These three conditions are discussed in more detail in the following sections.

2.1. Intrinsic High-Temperature Stability of the Photonic Structure

HTPS constituents need mechanical and chemical stability. They should be chosen such that their thermal expansion mismatch is low enough to avoid thermal stresses which lead to early structural failure (parameters for several materials are given in Table I). Chemical reactions between the components forming the photonic structure could degrade the photonic properties of the coating, reducing the thermal protection provided to the underlying materials and potentially leading to a temperature increase, an accelerated degradation, and finally an early failure of the whole system.

At high temperatures, new chemical phases having different thermomechanical properties can form between constituent layers and destabilize the photonic structure. One possible approach for overcoming the problems of chemical interaction between photonic structure constituents is to form the photonic structure by high-temperature segregation of two or more phases, causing the formation of nanoclusters or nanodomains. This approach was applied to incorporate paired-cluster rare-earth oxide dopants into zirconia, see for example.[12]

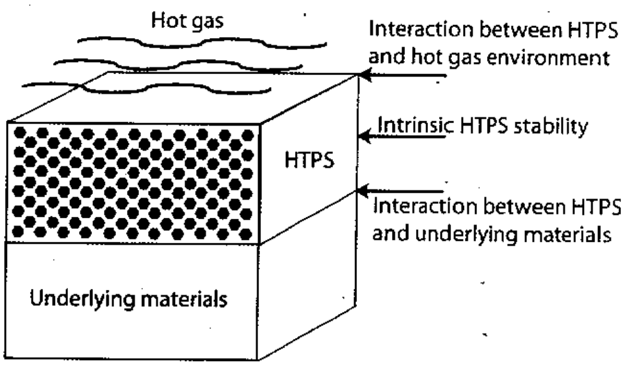

Fig. 1. Schematic presentation of the system substrate—high-temperature photonic structure (HTPS)—hot gas. The following types of high-temperature interactions must be considered when designing HTPS: (1) high-temperature intrinsic stability of the HTPS, (2) interaction of HTPS with hot gas environment, (3) interaction of HTPS with underlying material.

One of the profound problems in the application of Yttria Stabilized Zirconium (YSZ) for TBC applications is phase transformations, occurring in the parent ZrO_2. It has three polymorphic configurations: monoclinic, tetragonal, and cubic, stable at $T < 1170$ °C, $1170 < T < 2370$ °C, and $T > 2370$ °C, respectively. The volume contraction of ~5% during monoclinic-tetragonal transformation is sufficient for mechanical fracture of TBC.[13]

Photonic structures based on porosity modulation do not exhibit chemical and thermo-mechanical incompatibility. However, during high temperature operation, sintering and foreign object damage (FOD) can lead to a change of pores size and porosity distribution within the photonic structure that can reduce the thermal protection provided to the underlying materials.[14] The realization of oxide defect cluster (ODC) materials shows considerable promise in improving coating sintering resistance,[12, 15–17] Section 4.4.

Fibrous materials such as Ceramic Matrix Composites (CMC) could also be used to form the photonic structures. Design of the photonic behavior could be controlled by using weaving technology to adjust fiber dimensions and arrangement, while also taking advantage of the mechanical properties of a reinforced composite structure.[18] Various nanofibers have been produced with dimensions suitable for use in photonic structures, including transition-metal containing nanofibers,[19] SiO_2 nanofibers,[20] or TiO_2 nanowires.[21] But the subjecting CMC to high temperatures can significantly change the dimensions of the HTPS and by this means influence its band gap position. An estimation method of the elongation of fiber structure dimensions and thermal conductivity (TC) for fiber quartz ceramic structures was suggested.[22] As we will see in Section 6.2, stable fibers with regular diameter can be used for assembling two- and three-dimensional HTPS.

2.2. High-Temperature Interactions Between Photonic Structure and Hot Gas Environment

In one of the potentially most interesting applications of photonic structures, Thermally Protective Coatings (TBC), the heat source is a hot gas composed of combustion products. Depending on the fuel used, the composition of the hot gas can vary but usually contains NO_x, water coming from the combustion of either H_2 or fossil fuels, CO/CO_2, Unburned Hydrocarbons (UHC), and soot produced by combustion of fossil fuels. The gas can also contain impurities coming either from the fuel or through the air inlet. Commonly found impurities are sulfur, chlorine, vanadium, sodium, magnesium, potassium or calcium.[23] Water or corrosive products formed by impurities can react with the photonic structure leading to degradation of photonic properties and its early failure. To protect the photonic structure from the hot gas, a protective ceramic Thermal Environmental Barrier Coating (TEBC) could be deposited on the top of the photonic microstructure.

2.3. High-Temperature Interactions Between Photonic Structure and Underlayer Material

As an example of negative consequences of interactions between protective coatings and substrates, TBC in gas turbines can be considered, where failures occur at the interface between the TBC and alloy substrate. This interface contains a bond coat that increases adhesion between the two materials and provides elements that will oxidize at high temperatures. The oxidation of the bond coat gives birth to an oxide scale, called Thermally Grown Oxide (TGO), which acts as an environmental barrier preventing the underlying superalloy substrate from oxidizing. Upon thermal cycling, stresses develop due to a thermal expansion mismatch between the alloy, bond coat, TGO, and TBC layers, as well as due to the TGO growth. This can lead to crack nucleation, their subsequent growth and finally to the TBC delamination.[24]

Similar phenomena are likely to occur in other protective photonic structures due to the high thermal expansion of metallic substrates when compared to ceramics that compose the photonic structure. Moreover, thermal protection systems or high temperature functional structures are likely to have complex architectures comprising the photonic structure and some intermediate layers providing environmental protection, thermal protection, adhesion, or thermal stress accommodation; when designing the whole systems, interactions between all of these layers have to be considered.

Metallic photonic structures deposited on the metallic substrates should have few problems due to mismatch of coefficients of thermal coefficients expansion (CTE), but may require as discussed earlier deposition of the TEBC to protect the photonic structures from oxidation by hot gas components. The protective TEBC can be used in the temperature range of 1300 to 1400 °C, and for some advanced compositions up to 1650 °C (3000 °F).[25] Use of ceramic substrates for ceramic photonic structures could overcome some of these difficulties, but depending on the application, mechanical loads could become a problem. For this reason, the Ceramic Matrix Composites (CMC) have been considered a potential alternative for high temperature applications. Two types of CMC are usually considered: SiC-SiC CMC and oxide-oxide CMC. The former system has superior mechanical properties but is corrodible by water and therefore require protection by an environmental barrier.[26] Oxide-oxide CMC materials have shown higher resistance to water vapor corrosion at high temperatures, allowing their in simple designs.[27]

3. RADIATIVE HEAT TRANSFER AT HIGH TEMPERATURE

The energy of blackbody radiation emitted from a unit area in a unit time $E_b(T)$ obeys the Stefan-Boltzmann law.

$$E_b(T) = \sigma T^4 \tag{1}$$

The heat radiation is more efficient with increasing temperature. We shall see in this Section that this concerns temperatures of 1000 °C and higher. The emitted IR radiation is distributed over some interval according to Planck's law.

$$u(\omega, T) = \frac{8\pi\hbar\omega^3}{c^3}\frac{1}{e^{\hbar\omega/k_BT}-1} \tag{2}$$

Here ω is the photon frequency, u is the radiation energy per unit frequency interval per unit volume, and σ and k_B are the Stefan-Boltzmann and Boltzmann constants, respectively. The position of the peak of this distribution obeys the Wien's law

$$\lambda_{\max} T = 2897.8\ \mu\text{m} \cdot \text{K} \tag{3}$$

These equations should be modified for photonic crystals (Section 6), where the dispersion of light is nonlinear. In this section however, we consider the heat transport in a common blackbody, assuming the linear dispersion law $\omega = ck$ (where k is the photon's wave vector).

Let us begin our consideration with the general expression for thermal conductivity:

$$\kappa_r = \frac{1}{3} C_V S l \tag{4}$$

Here C_V is the heat capacity per unit volume, S is velocity of the particles, which are responsible for the heat transport, and l is their mean free path. The radiation component of the heat conductivity is due to photon propagation. Therefore, $S = c/\sqrt{\varepsilon}$ is the velocity of light in the media, ε is the dielectric constant, and l is the mean free path (MFP) of photons. Taking into account the dependence of these values on the photon frequency, we write the expression for radiation thermal conductivity (RTC) as follows:

$$\kappa_r = \frac{c}{3\sqrt{\varepsilon}} \int_0^\infty C_V(\omega) l(\omega) d\omega$$
$$\text{where } C_V(\omega) = \frac{\hbar}{\pi^2 c^3}\frac{\partial}{\partial T}\left(\frac{\omega^3}{e^{\hbar\omega/k_BT}-1}\right) \tag{5}$$

Behavior of the integrand at small frequencies is very important for the integral value. Indeed, if we assume that the mean free path (MFP) is determined by the structure disorder, then the MFP should follow the Rayleigh law $l(\omega) \propto \omega^{-4}$, $C_V(\omega) \propto \omega^2$, and the integrand (5) has a singularity at $\omega \to 0$.

This dependence has been discussed in paper.[28] It was shown that bulk mechanisms of light absorption prevail at small frequencies. They could arise from either the interaction of light with optical phonons or the electron-photon interaction. In the latter case the effect should essentially depend on temperature and the density of defects, which serve as the donors of free electrons at high temperatures. The simplest way to take this fact into account has been suggested in Ref. [27]. The authors introduce the cutoff frequency ω_A, assuming $l(\omega) = 0$, if $\omega < \omega_A$. Here ω_A is the absorption edge frequency, which can be measured. For example for the Yttria-Stabilized Zirconia (YSZ), $\omega_A/2\pi = 6 \times 10^{13}$ Hz.[28] Thus, the equation for RTC can be written as:

$$\kappa_r = \frac{20\sigma\varepsilon}{\pi^4} T^3 \int_{\Theta_A/T}^\infty \frac{x^4 e^x}{(e^x-1)^2} l(x)\,dx, \quad \text{where } x = \frac{\hbar\omega}{k_B T} \tag{6}$$

and $\Theta_A = \hbar\omega_A/k_B$. The dependence of $x^4e^x/(e^x-1)^2$ on the non-dimensional frequency x is presented in Figure 2. We see that this factor in the integrand is significant over the frequency interval

$$2k_BT/\hbar < \omega < 8k_BT/\hbar \tag{7}$$

The radiation component is most important, if this interval belongs to the frequencies above cutoff, $\omega > \omega_A$. For YSZ this corresponds to $T > 1500$ K.

The absorption coefficient of oxide materials used for the fabrication of TBC is very important in the interval up to about $\lambda = 5\ \mu$m, which is characteristic of the engine operation temperature. The ZrO_2 coatings can have low absorption coefficients, as shown in Figure 3.[10] Generally, zirconia materials are translucent to thermal radiation in relevant wavelength range.

The structure disorder reduces the MFP l of photons, and, therefore, reduces the thermal conductivity. The effect depends on relation between the characteristic size d of the disorder and the photon wavelength λ. If $d \ll \lambda$, the media can be considered as homogeneous on average. This effective media can be obtained after averaging the optical constants over the scale of the light wavelength. The scattering occurs due to deviation of the local optical constant from the average ones. It is very small for $l \gg \lambda$, and it obeys Raleigh's law. This scattering obeys the Mie law and will be considered in Section 8. In general, we can assume

$$\frac{1}{l} = \frac{1}{l_{\text{small}}} + \frac{1}{l_{\text{large}}} \tag{8}$$

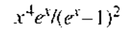

Fig. 2. Dependence of the function $x^4e^x/(e^x-1)^2$ on non-dimensional frequency x.

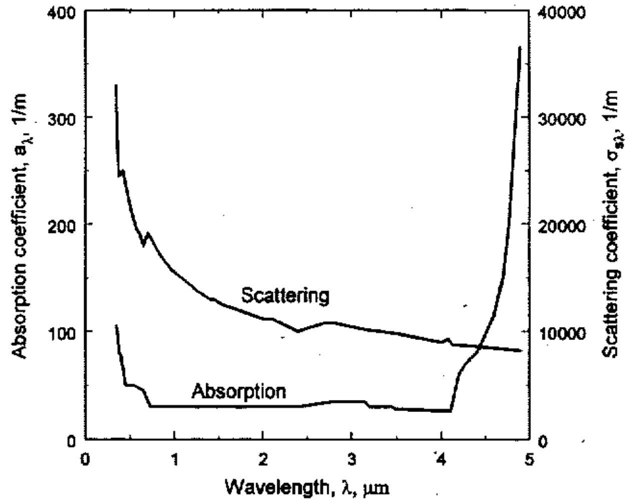

Fig. 3. Spectral absorption and scattering coefficients for zirconia. Reprinted with permission from [10], R. Siegel and C. M. Spuckler, *Mater. Sci. Eng. A* 245, 150 (**1998**). © 1998, Elsevier.

where l_{small} and l_{large} are MFP values obtained in Sections 7 and 8 respectively. An error can arise from pores of intermediate size ($d \approx \lambda$), when they comprise a considerable part of total porosity.

4. 1D HIGH-TEMPERATURE PHOTONIC STRUCTURES

In photonic structures, the dielectric permittivity $\varepsilon_r(\boldsymbol{r})$ modulation governs the photonic band gap that is a prerequisite for the HTPS properties. This is expressed by Maxwell's equations and the wave equation that follows from them:[3]

$$\nabla \times [\nabla \times E(r)] = \frac{\omega^2}{c^2}\varepsilon_r(r)$$

Let us consider the modulation of dielectric permittivity $\varepsilon_r(\boldsymbol{r})$ in a multilayer 1D HTPS, which can be achieved in different ways including composition modulation, density modulation, and porosity modulation.

The function of a one-dimensional HTPS has a dependence on its location with respect to an emitter, for example heated substrate. This dependence was studied theoretically in Ref. [31], Figure 4. The quantitative results (thermal power spectrum) were obtained for a one dimensional PBGM (quarter-wave stack), and were extended to two and three-dimensional PBGM using qualitative approach, based on the model by John and Wang.[32] For the one-dimensional case, if the lossless hotplate is above a heated hotplate, the quarter-wave stack can play the role of an antireflection coating or passive filter at the band gap

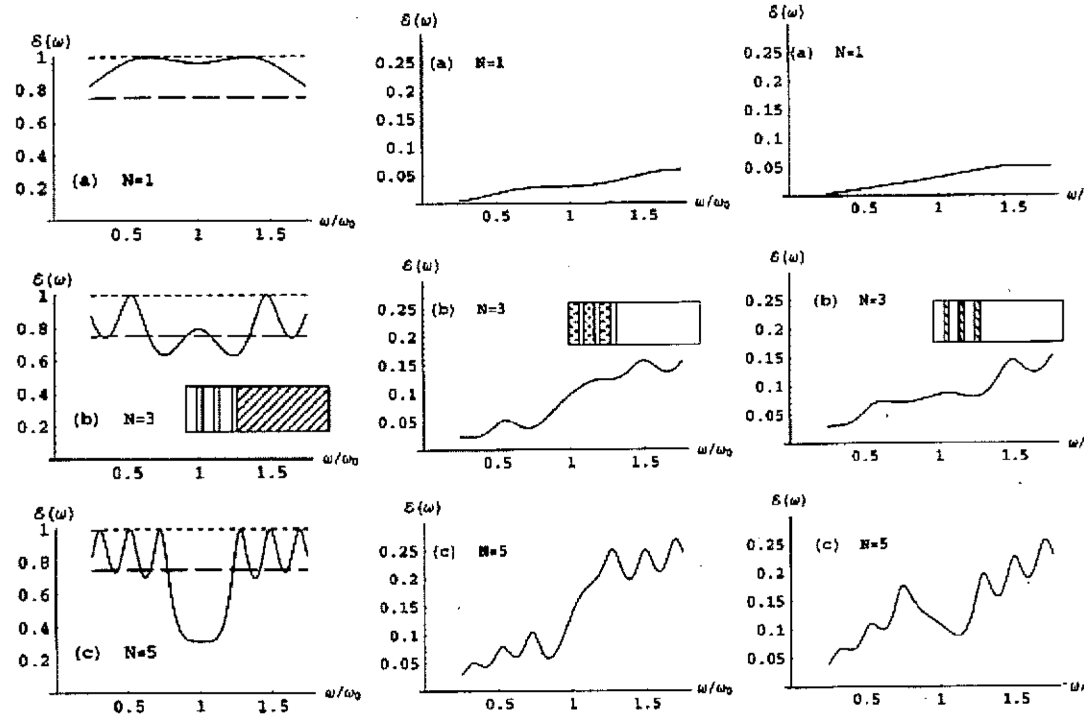

(a) (b) (c)

Fig. 4. Calculation results, illustrating emissivity $\varepsilon(\omega)$ as a function of scaled frequency ω/ω_0 for three different locations of the PBGM with respect to the heated substrate as a function of the number of periods N. (a) The emissivity of substrate ($n = 3 + 0.03i$) coated by a lossless PBGM film ($n_1 = \sqrt{2}$, $n_2 = 2$). Dotted line is emittance of perfect blackbody substrate, dashed line is gray-body emittance of substrate. (b) Substrate is lossless, $n_3 = 1$, absorbers are located in the absorption region $n_1 = \sqrt{2} + i\sqrt{2}/100$ with $n = 2$ losses. (c) Absorbers are located in the high-index layers $n_2 = 2 + 0.02i$ with $n_1 = \sqrt{2}$ and $n_3 = 1$ lossless. Reprinted with permission from [31], C. M. Cornelius and J. P. Dowling, *Phys. Rev. A* 59, 4736 (**1999**). © 1999, American Physical Society.

frequency, as shown in Figure 4(a). This effect becomes stronger with an increase in the number of periods N. If the emitters are moved from the substrate into PBGM layer, active enhancement and suppression may occur, depending on location of emitters in the low (n_1) or high index (n_2) regions. If emitters are in the low index region, emission enhancement is highest at the high frequency band edge, as in Figure 4(b). If emitters are in the high index layers, the emission enhancement is strongest at the low frequency band edge, as in Figure 4(c).

Consider the normal propagation of light through an infinite 1D "sandwich" structure with layer parameters (ε_1, d_1), (ε_2, d_2), (ε_1, d_1), $(\varepsilon_2, d_2), \ldots$, as in Figure 5. Let $k_1 = \omega\sqrt{\varepsilon_1}/c$ and $k_2 = \omega\sqrt{\varepsilon_2}/c$ be the wave vectors of light in the appropriate layers, where k is the Bloch wave vector. This problem is similar to the well known Kronig-Penney model for electrons in a 1D periodic structure of square barriers. The relation connecting k and ω is

$$\cos k(d_1+d_2) = \cos k_1 d_1 \cos k_2 d_2 - \frac{k_1+k_2}{2k_1k_2}\sin k_1 d_1 \sin k_2 d_2 \tag{9}$$

This equation determines the dispersion of light in the structure. At small k we have a linear dispersion law

$$\omega = Sk, \quad \text{where } S = c\frac{d_1+d_2}{\sqrt{\varepsilon_1 d_1^2 + \varepsilon_2 d_2^2 + (\varepsilon_1+\varepsilon_2)d_1 d_2}}$$

For $k_1 = k_2$ (in the homogeneous media), Eq. (9) reduces to $\cos k(d_1+d_2) = \cos k_1(d_1+d_2)$, and we obtain a primitive dispersion law $k = k_1 = \omega\sqrt{\varepsilon_1}/c$. For $k_1 \neq k_2$ the result depends on the right side of Eq. (9). The expression $(k_1^2+k_2^2)/2k_1k_2$ is always greater than unity. This means that the right side of Eq. (9) can be either less than or greater than unity. If it is less than unity, then Eq. (9) yields a real value for k, which corresponds to the extended state of the photon. If

$$\left|\cos k_1 d_1 \cos k_2 d_2 - \frac{k_1^2+k_2^2}{2k_1k_2}\sin k_1 d_1 \sin k_2 d_2\right| > 1$$

then k is imaginary, and, therefore, the photonic state is not extended; we are in the band gap.

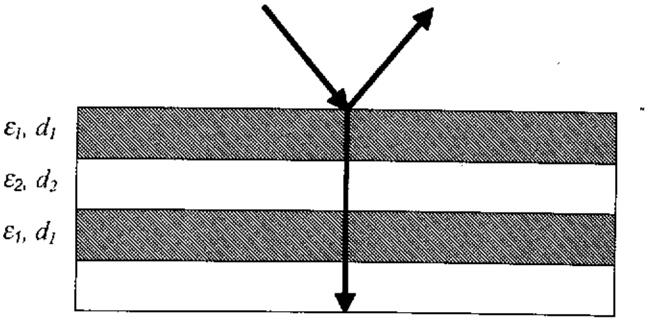

Fig. 5. Normal propagation of light through an infinite one dimensional "sandwich" (ε_1, d_1), (ε_2, d_2), (ε_1, d_1), $(\varepsilon_2, d_2), \ldots$

Assuming $k_1 \approx k_2$, and thereby $\varepsilon_1 \approx \varepsilon_2$, we can roughly estimate the gap size as

$$\Delta \approx \frac{2c|n_2-n_1|}{n_1d_1+n_2d_2}\left|\sin\frac{\omega n_1 d_1}{c}\right| \tag{10}$$

The value of a right side of Eq. (9) is presented in the Figure 6(a). The regions, where this function is outside the region $[-1, 1]$, correspond to the gap. In Figure 6(a) these regions are $[1.8, 2.4]$ and $[4.0, 4.4]$.

Analyzing Eq. (9) shows that wider gaps can be expected if $k_2 \gg k_1$ while $k_1 d_1 \approx k_2 d_2$, as shown in Figure 6(b). In this case, estimation from Eq. (9) yields

$$\Delta \approx \left(\pi - 2\sqrt{\frac{2n_1}{n_2}}\right)\frac{c}{n_1 d_1} \tag{11}$$

Equations (9)–(11) can easily be generalized for estimation of the band gap position and band gap width for oblique light incidence as a function of the thickness and dielectric constants of individual layers. It is apparent that to create a large gap photonic crystal, we have to choose materials with highly contrasting refraction indexes.

4.1. Multilayers with Composition Modulation

Multilayered HTPS with refraction index modulation (HTPS-RM) have been proposed for thermophotovoltaic applications.[33] The authors have investigated a one-dimensional Si/SiO$_2$ photonic crystal ($n(\mathrm{SiO_2}) \approx 1.5$,

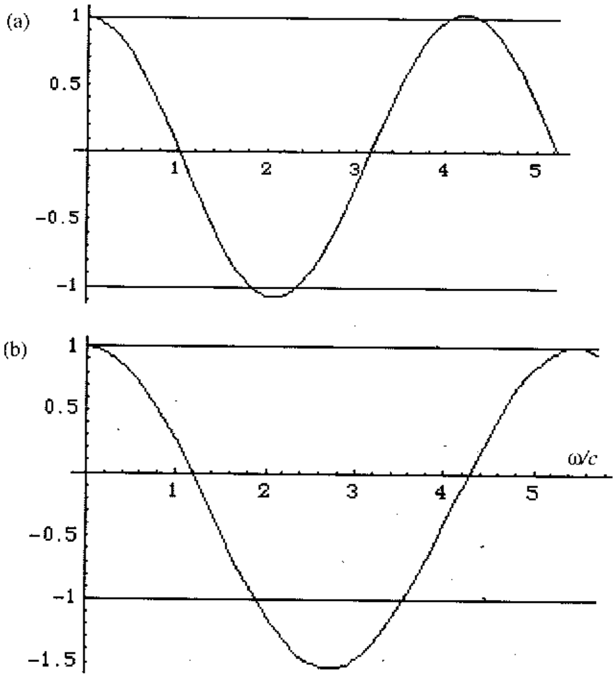

Fig. 6. Estimation of gap size using equations (10) and (11). (a) Right part of (9) for $d_1 = d_2 = 0.5$, $n_1 = 1.2$, $n_2 = 1.8$. Estimation (10) yields $\Delta = 0.3$. (b) Right part of (9) for $d_1 = 0.5$, $d_2 = 0.2$, $n_1 = 1.1$, $n_2 = 3$. Estimation (11) yields $\Delta = 4$.

$n(\mathrm{Si}) \approx 4$) as presented on Figure 7(a). They found good agreement between the measured reflectance and the modeling estimate, Figure 7(b).

In TBC studies, two strategies were used for deposition of alternating layers with different chemical composition (and different refraction index):[6] (a) deposition of layers with constant layer thickness (400 nm for 7YSZ layers and 100 nm for Al_2O_3 layers), and (b) deposition of layers with variable layer thickness (from 740 nm for 7YSZ and 765 nm for Al_2O_3 near the substrate with the increment of 5 nm to 90 nm for 7YSZ and 115 nm for Al_2O_3 near the coating surface). Preliminary results show, that the IR reflection spectrum of the coating in Figure 8 with variable layer thickness (from 1 to 2.75 μm) is significantly broader in bandwidth than the coating with constant layer thickness (73% at 1.85 μm), and both multilayer coatings have much broader reflection spectrum than a monolithic coating, as shown in Figure 9. Multilayer coatings with controlled refraction indices and thicknesses can be used to reach a desired reflectance in a desired wavelength range.

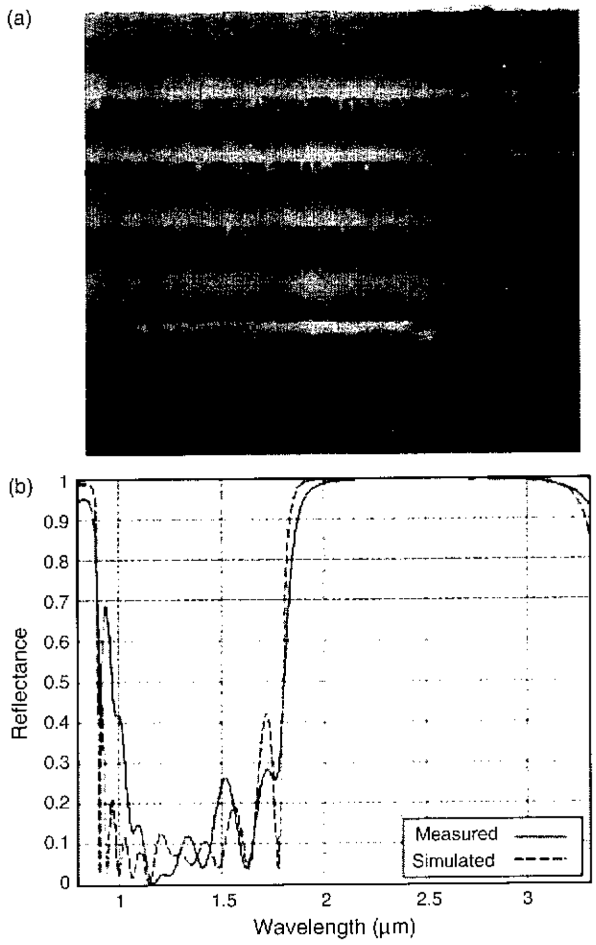

Fig. 7. A one-dimensional Si/SiO_2 photonic crystal with arc-deposited SiO_2 layer. (a) TEM cross-section. (b) Measured and simulated normal incidence reflectance spectra. Reprinted with permission from [33], F. O'Sullovan et al., *J. Appl. Phys.* 97, 033529 (**2005**). © 2005, American Institute of Physics.

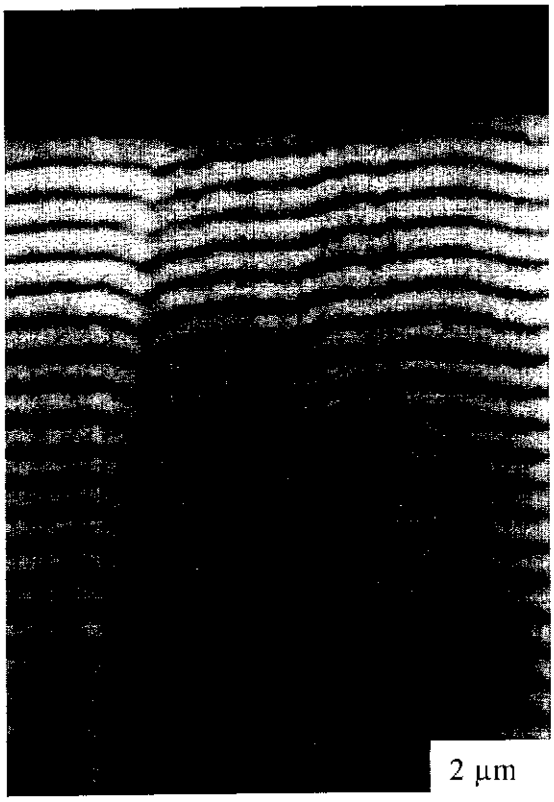

Fig. 8. SEM image of a variable layer thickness Al_2O_3/7YSZ coating. Reprinted with permission from [6], M. J. Kelly et al., *Int. J. Appl. Ce Technol.* 3, 81 (**2006**). © 2006, Blackwell Publishing.

4.2. Multilayers with Density Modulation

Electron Beam Physical Vapor Deposition (EB-PVD) YSZ coatings have columnar morphology with a large grain size of 100–250 μm and a significant preferred orientation in the middle of the coating, and a smaller grain size of 5–10 μm with no preferred orientation close to the bond coat, depicted in Figure 10(a).[34] Plasma Spray

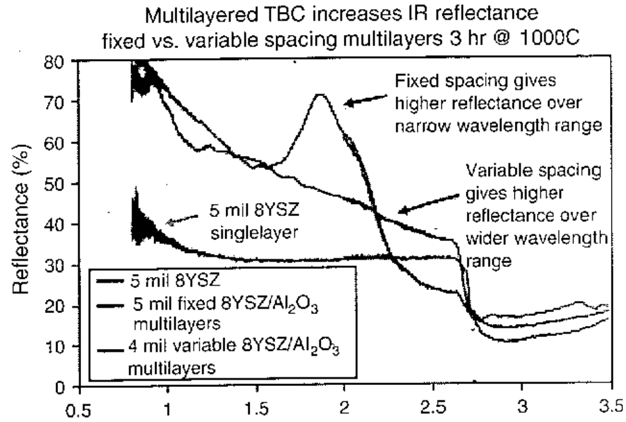

Fig. 9. Comparison of the hemispherical reflectance of coatings with variable layer thickness, fixed layer thickness, and an 8YSZ monolayer. Reprinted with permission from [6], M. J. Kelly et al., *Int. J. Appl. Cer. Technol.* 3, 81 (**2006**). © 2006, Blackwell Publishing.

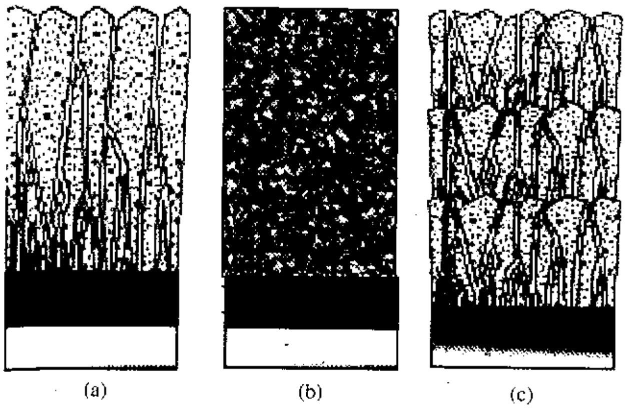

Fig. 10. Scheme illustrating the typical microstructure of YSZ coatings. (a) Columnar EB-PVD coating. Grain size is 100–250 μm in the middle of coating, 1–2 μm close to the substrate. Preferred orientation is clearly seen. (b) APS coating. Splat morphology is schematically shown. Splats are separated by microcracks and pores. (c) Multilayer EB-PVD coating, deposited using the *"in-and-out"* method (Figures (a) and (c) are taken from [34]). Reprinted with permission from [34], J. Singh et al., *Mater. Sci. Forum* 455–456, 579 (**2004**). © 2004, Scientific.Net.

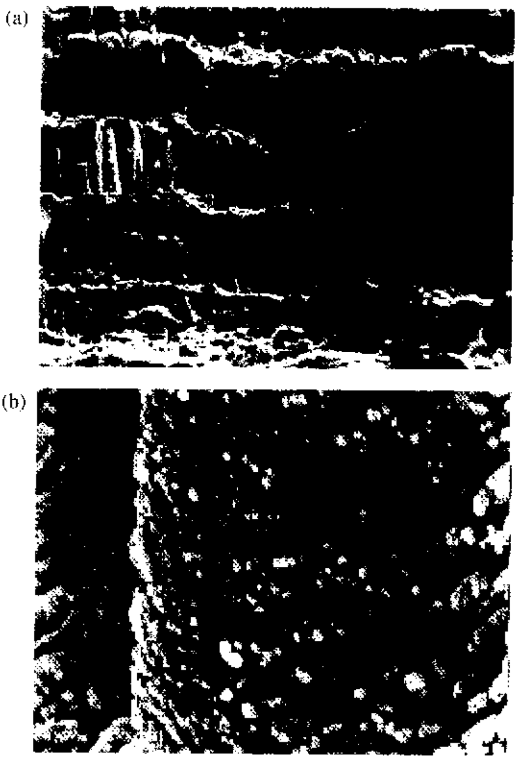

Fig. 11. SEM fracture patterns of 8YSZ deposited with density modulation (HTPS-DM). (a) Multilayer coating obtained with *"in-and-out"* method. (b) 40-Layer coating obtained with *"shutter"* method [SiO_4]. Reprinted with permission from [34], J. Singh et al., *Mater. Sci. Forum* 455–456, 579 (**2004**). © 2004, Scientific.Net.

(PS) coatings have splat morphology with a splat thickness of 1–2 μm, as in Figure 10(b). New multilayer coatings, recorded in papers,[6, 34, 35] have morphology somewhere between columnar and splat as shown in Figure 10(c). This hybrid coating morphology provides coating density modulation (HTPS-DM). In the case of regular periodicity normal to the substrate, radiative and phonon thermal conductivity decrease due to the presence of intersplat microcracks and intersplat porosity.

As one would expect, the interfaces between the layers are very sharp in EB-PVD coatings deposited using the *"in-and-out"* method (periodic translation of the sample away from the vapor cloud) and diffuse in coatings deposited using the *"shutter"* method (periodic vapor flow interruption during deposition) as illustrated in Figure 11. In the latter case, microporosity near interfaces provide frontiers between layers. Measurements of thermal conductivity and hemispherical reflectance of multilayer coatings of both types confirm this suggestion.

Multilayer YSZ and HfO_2-26 wt% Y_2O_3 materials obtained by *"in and out"* and *"shutter"* methods[6, 35] can be also considered as an example of HTPS-DM because the refraction indexes of HfO_2 and ZrO_2 are very close. The hemispherical reflectance of the multilayered *"in and out"* multilayer at 1 μm wavelength increases from $\approx$50% to $\approx$63% and to $\approx$78% when going from a 1-layer to a 10-layer and to a 40-layer structure. At the same wavelength, the hemispherical reflectance of *"shutter"* materials increases from 35% to 45% for 1-layer and 20-layer respectively, shown in Figure 12. The difference in reflectivity between *"in and out"* and *"shutter"* methods was explained by the sharper interface and coating thickness of the *"shutter"* method.

Individual layers in multilayer HTPS-DM obtained by both *"in and out"* and *"shutter"* methods differ from single layer bulk materials by many morphology features, leading to a significant decrease of phonon thermal conductivity. Local strain energy fields, lattice mismatch, surface restructuring, presence of extended interfaces and microporosity provide reason enough to distinguish them from HTPS-PM (Section 4.3).

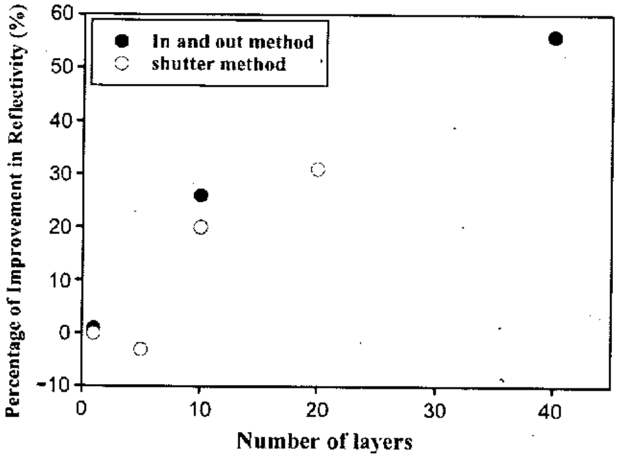

Fig. 12. Improvement of hemispherical reflectance with an increase in the number of layers in an HTPS-DM type structure of EB-PVD YSZ. Reprinted with permission from [35], D. E. Wolfe et al., *Surf. Coat. Techn.* 190, 132 (**2005**). © 2005, Elsevier.

It is important to note, that HTPS-DM have distinct advantages over HTPS-CM, TTPS-PM and monolayer HTPS. First, there is no variation of the coating chemical composition and structures with coating thickness. Second, it is possible to lower the thermal conductivity. Finally, it is easier to accommodate the mismatch between the coefficients of thermal expansion (CTE) due to temperature change.

4.3. Multilayers with Porosity Modulation

Modulation of porosity can be used as a possible mechanism for refractive index modulation. Suppose the pore size is small in comparison with the wavelength of light $\lambda = \pi\hbar c/2k_BT$. This allows us to introduce an effective permittivity of the porous media and relate it to the porosity p_i of each layer i $(i = 1, 2)$.

$$\varepsilon_i = p + (1-p)\varepsilon - \frac{p_i(1-p_i)(\varepsilon-1)^2}{3[p+(1-p)\varepsilon]} \qquad (12)$$

Equation (12) is the particular case of the effective permittivity of a mixture.[36] It can also follow from Eq. (32), later in this paper. Equation (10) can then allow us to express the gap value of the HTPS via structure porosity. Assuming $\omega = 4k_BT/\hbar$ and $\omega n_1 d_1/c \sim 1$, we find that the gap is on the order of $|p_2 - p_1|n \cdot 4k_BT/\hbar$, where $n = \sqrt{\varepsilon}$ is the refraction index of the dense material.

Since $|p_2 - p_1| < 1$, the effect can only be expected in materials with high refraction index. We know nothing about experiments on such materials at high temperatures. Nevertheless, peculiarities of the photonic bands of structures with porosity modulation have been observed in the reflection spectra of porous silicon. Figure 13 presents the structure used in paper.[37] Porosities of the layers are 50% and 75% (80%), corresponding to refractive indexes of 2.15 and 1.43 (1.32), respectively. The reflectance spectrum of the structure is presented in Figure 14. The authors observed a blue shift in the spectrum due to oxidation of silicon at 900 °C over a time span of 10 min. Other results showed that porous SiO_2 obtained after oxidation of Si at 800 °C can be used for developing a rainbow-like band filter.[38]

A periodic alternation of two different current densities can be used to fabricate multilayer porous silicon structures.[39] The technique makes it possible to grow one dimensional photonic structures with porosities varying between 44% $(n = 2.3)$ and 85% $(n = 1.2)$. These structures could be used as mirrors as in Figure 15(a), or filters, as in Figure 15(b). The transmission spectrum of the structure on Figure 15(a) is presented in Figure 16.

Great care must be taken in order to reliably predict the lifetime of porous structures, as a result of well known changes in microstructure due to high temperature ceramic sintering and densification, as discussed in Sections 2.1 and 4.4.

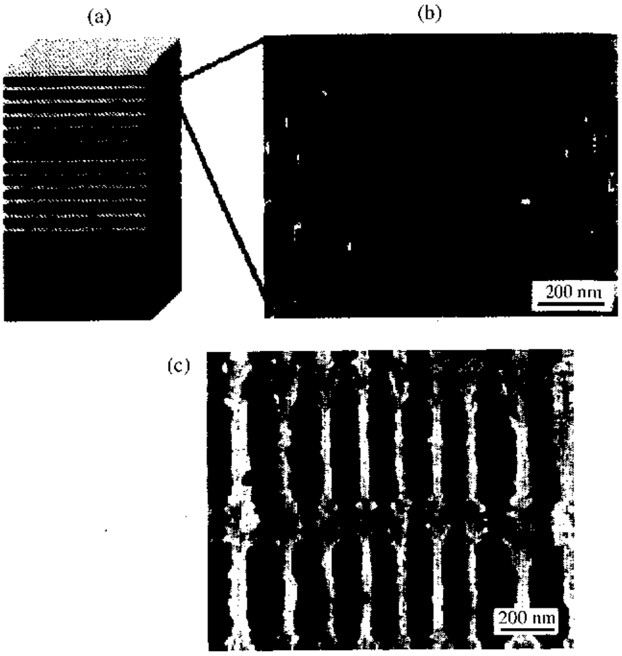

Fig. 13. An example of porous structure with porosity modulation. (a) Schematic of a porous silicon nanostructure. Yellow and red colors represent layers of high (lower refraction index) and low (high refraction index) porosity, respectively; (b) and (c) are the SEM images of mesoporous and macroporous silicon layers. Reprinted with permission from [37], S. Weiss et al., *Optics Express* 13, 1090 (**2005**). © 2005, Optical Society of America.

4.4. Multilayers with Atomic Mass Modulation

The oxide defect cluster (ODC) design approach was successfully applied for obtaining advanced TEBC with significantly reduced long-term TC.[12, 15–17] The modulation of deposition conditions, described in Section 4.2 for multilayer YSZ and HfO_2-26 wt% Y_2O_3 materials ("in and out" and "shutter" methods[6, 35]) could be used for fabrication of multilayers with atomic mass modulation (concentration of ODC within separate layers, alternating with "normal" TBC layers). To obtain ODC,

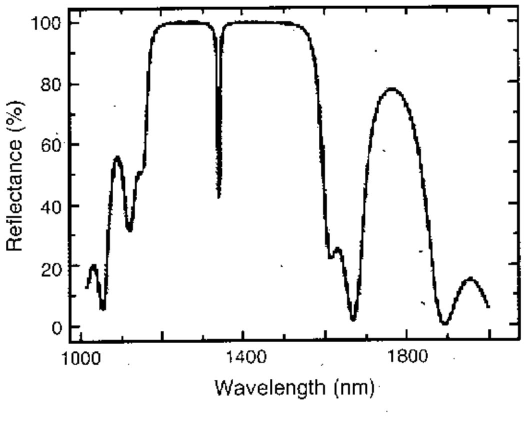

Fig. 14. Reflectance spectrum of the structure shown in Figure 13. Reprinted with permission from [37], S. Weiss et al., *Optics Express* 13, 1090 (**2005**). © 2005, Optical Society of America.

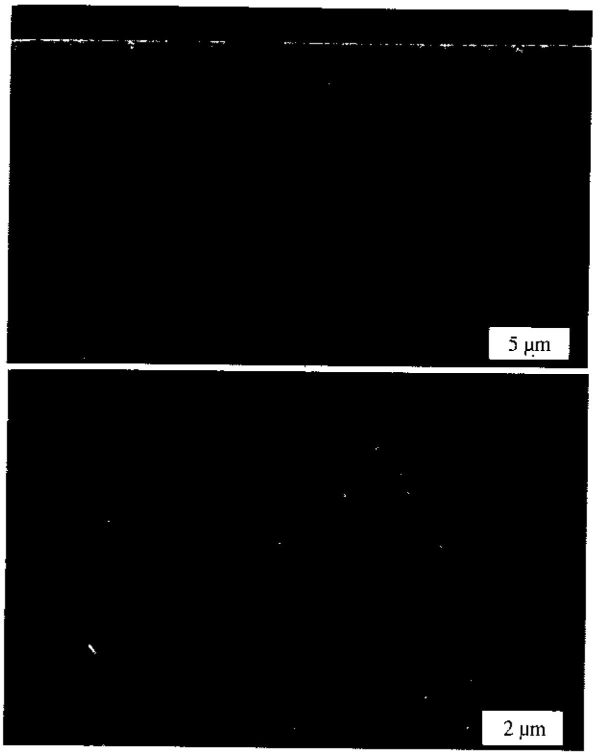

Fig. 15. Porous multilayer Si structure, fabricated by alternating the current density. (a) Cross-section SEM image of mirror structure. (b) Cross-section SEM image of filter structure. Reprinted with permission from [39], M. Qian et al., *J. Cr. Growth* 292, 347 (**2006**). © 2006, Elsevier.

Fig. 17. TEM pattern showing Nd-, Yb-, Sc-induced ODC (arrows) in plasma-sprayed ZrO_2-6 mol% (Y, Nd, Yb, Sc$)_2O_3$ coating. Reprinted with permission from [16], D. Zhu et al., NASA/TM-2004-212480, January (**2004**). © 2004, NASA.

the EB-PVD method was used. The incorporation of multidopant paired-cluster rare-earth oxides into the parent ZrO_2-Y_2O_3 system was performed based on the analysis of interatomic and chemical potentials, lattice strain energy, polarization and electro-neutrality of the whole oxide system. As an example of an advanced TEBC, the coating system included ZrO_2-Y_2O_3-Nd_2O_3(Gd_2O_3, Sm_2O_3)-Yb_2O_3(Sc_2O_3) on NiCrAlY or PtAl, with EB-PVD deposited onto superalloy or mullite/mullite + barium strontium aluminosilicate (BSAS)/Si coated SiC/SiC CMC substrates.[25] The TEM studies indicate the presence of the 5 to 100 nm sized ODC and nanophases in PS 13.5% (Y, Nd, Yb$)_2O_3$ and EB-PVD ZrO_2-12 to 14% (Y, Gd, Yb$)_2O_3$,[16] see Figure 17. The segregation of ODC can be considered to be responsible for the observed significant reduction of TC and improved high-temperature sintering resistance. It is essential to stress that the real time monitoring of TC under realistic engine-like conditions of temperature and heat flux were used for creation and study of ODC structures. The formation of ODC, as one of the approaches to thermodynamically stable structures with controlled defect size, is the way to effectively attenuate and scatter phonons as well as radiative photons in a wide spectrum of frequencies.[12, 15–17, 25] On the other hand, it is important to keep in mind that the TC and the TC rate in ODC systems show a clear minimum for the ODC concentration of about 10 mol% of total dopant content. The start and character of ODC formation can be related to the position of phase composition boundary between tetragonal ZrO_2 and cubic ZrO_2.[12] Further studies of ODC formation must be accompanied by more detailed observation (also

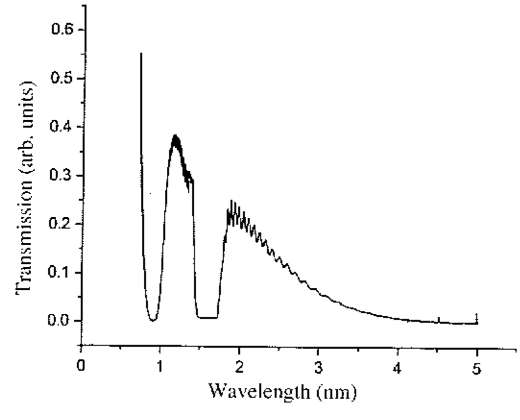

Fig. 16. Transmission spectrum of the structure shown in Figure 15(a). Reprinted with permission from [39], M. Qian et al., *J. Cr. Growth* 292, 347 (**2006**). © 2006, Elsevier.

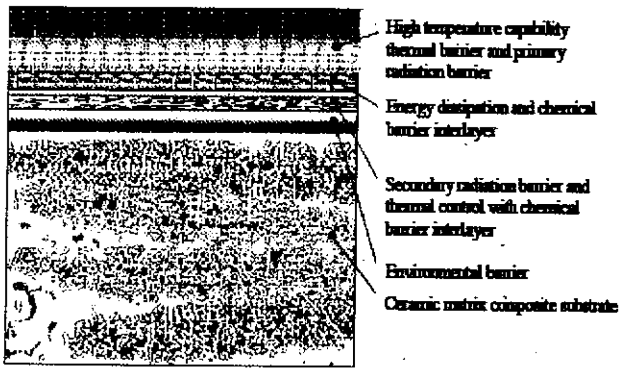

Fig. 18. An example of the concept TEBC system at 1650 °C for ceramic matrix composition (CMC) combustor and vane applications. Reprinted with permission from [25], D. Zhu and R. A. Miller, NASA/TM-2004-213129, August (**2004**). © 2004, NASA.

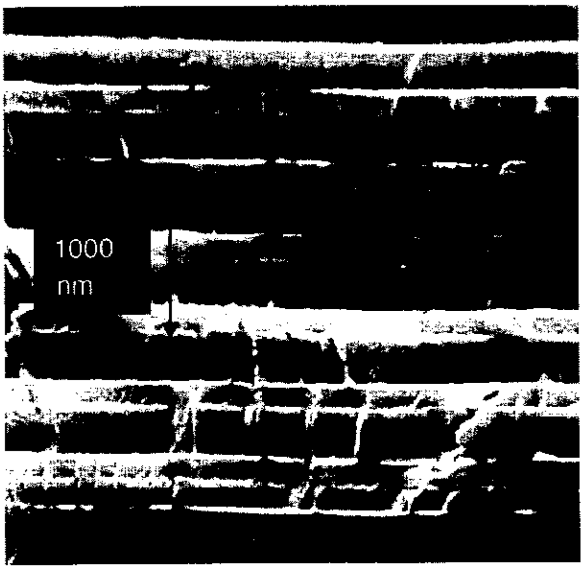

Fig. 19. ODR film, representing a 14-layer Fibonacci sequence of high and low refraction index layers (Si and SiO_2). SEM fracture pattern. The film was deposited using pulsed DC magnetron sputtering. Reprinted with permission from [9], D. Lusk and F. Placido, *Thin Solid Films* 492, 226 (2005). © 2005, Elsevier.

with TEM) of the high-temperature phase transformation in the parent ZrO_2 (or stabilized YSZ).[40] A possible concept of advanced TEBC system for 1650 °C is shown on Figure 18.

4.5. Quasiperiodic Dielectric Stacks

An omnidirectional reflector (ODR) in the IR wavelength range (centered at 1540 nm), based on a Fibonacci sequence (FS) of high and low refraction index layers was modeled and fabricated.[19] This ODR has a 14-layer structure [substrate/$(ABA)^6$ A_{top}/air], where A is low and B is high refraction materials (Si and SiO_2 respectively, Fig. 19, Table I). A top layer of low refraction index material A_{top} with thickness d_{top} was introduced. The thicknesses of layers $d_A = d_B = 139.3$ nm and $d_{top} = 98$ nm were found in an ODR with bandwidth 1437–1618 nm = 181 nm at $R_{min} = 99.5\%$. The observed small reduction of R_{ODR} can be explained by the absorption in Si layers. It was also shown that the maximum possible ODR bandwidth $\Delta_\lambda =$ 384 nm from 1380 nm to 1764 nm was found for 28 periods, leading to significant increase of coating thickness from 2.61 to 11.7 μm. The authors report a significant dependence of reflectivity on the incidence angle. This dependence is most pronounced at non-normal incidence, where appreciable dependence on polarization is observed.

5. 2D HIGH-TEMPERATURE PHOTONIC STRUCTURES

Modulation of the refraction index can be caused by modulating the dielectric permittivity, magnetic permeability or both. In Section 4 we considered the one dimensional modulation of the refraction index. Here we shall generalize this consideration on the 3D photonic crystal, assuming 2D PC as the particular case. Let us restrict ourselves to nonmagnetic materials assuming $\mu = 1$ and $\varepsilon(\boldsymbol{r})$ to be a periodic function of $\boldsymbol{r}$.

Consider the problem of light propagation in a photonic crystal. Maxwell's equations for the electrical field can be reduced to

$$\Delta \boldsymbol{E}(\boldsymbol{r}) + \frac{\omega^2}{c^2}\varepsilon(\boldsymbol{r})\boldsymbol{E}(\boldsymbol{r}) = 0 \qquad (13)$$

This equation resembles the Schrödinger's equation with the periodical "potential" $\varepsilon(\boldsymbol{r})\omega^2/c^2$ and vector "wave function" $\boldsymbol{E}(\boldsymbol{r})$. Therefore, its solution obeys the Bloch theorem:

$$\boldsymbol{E}(\boldsymbol{r}) = \sum_{\tau} e^{\tau} E_k^{\tau}(\boldsymbol{r}) e^{ikr} = \sum_{G,\tau} \boldsymbol{e}^{\tau} \tilde{E}_k^{\tau}(\mathbf{G}) e^{i(k+G)r} \qquad (14)$$

Here $E_k^{\tau}(\boldsymbol{r})$ is a Bloch amplitude: this is a periodic function of $\boldsymbol{r}$, which has been expanded into a Fourier series, $\tau =$ 1, 2 is the polarization index, $\boldsymbol{e}^{\tau}$ is the unit vector of the polarization, and $\boldsymbol{G}$ is the reciprocal lattice vector. Tilde denotes the Fourier transform of the corresponding value. We can write

$$\varepsilon(\boldsymbol{r}) = \sum_{G\in \mathrm{BZ}} \tilde{\varepsilon}(\boldsymbol{G}) e^{iGr}, \quad \text{where } \tilde{\varepsilon}(\boldsymbol{G}) = \frac{1}{V}\int_V \varepsilon(\boldsymbol{r}) e^{-iGr} d^3r \qquad (15)$$

Inserting of Eqs. (14) and (15) into Eq. (13) results in an eigenvalue problem, solution of which yields the photonic band spectrum. The field in the photonic crystal is shown in Figure 20, and its photonic spectra are shown in Figure 21.

In these figures, we examine a realistic photonic coating. Real coatings must consist of a finite number of layers. For demonstration, we examine a five layer structure consisting of large holes in a dielectric, though more would be used in practice. In the horizontal dimension, the structure is infinitely periodic.

We assume a hypothetical material with a high relative permittivity of 9. This allows us to achieve a narrow bandwidth complete band gap in the case of an infinite photonic crystal, as shown in the band diagram, where overlapping E_z and H_z band gaps ensure that no light, regardless of polarization, can propagate in the material. In the band diagram, the blue color represents the E_z polarization, and red represents the H_z polarization. For the material parameters and hole radius used (radius = 0.48 ∗ lattice constant), we obtain the complete band gap shown in purple.

The Poynting power patterns shown in Figure 20 represent wavelengths below, within, and above the E_z band gap between the third and fourth E_z bands, at 3750, 4000, and 4300 nm respectively (corresponding to normalized frequencies of 0.533, 0.5, and 0.465), of an normally incident E_z polarized wave.

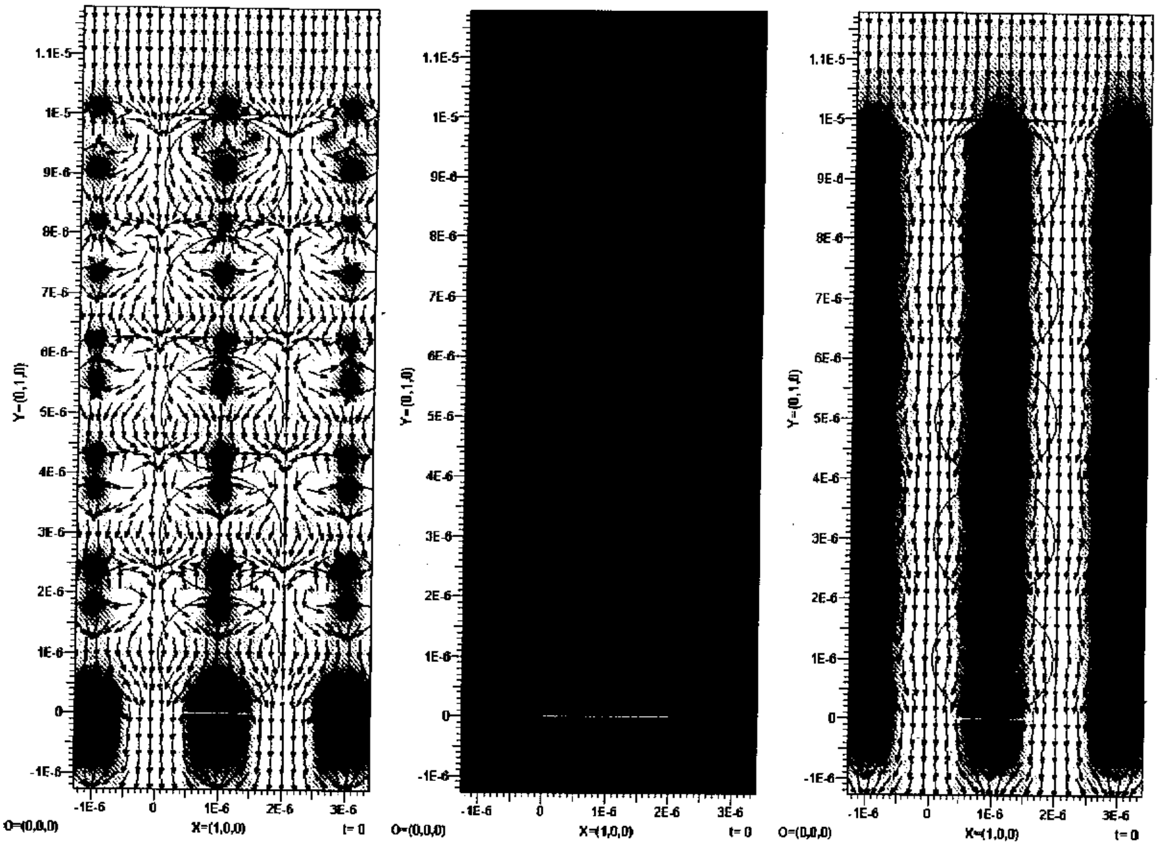

Fig. 20. Poynting power distribution for the E_z modes of a five layer photonic crystal structure excited by a normal incidence source with wavelengths of 3750, 4000, and 4300 nm, corresponding wavenumbers just under, within, and just beyond the band gap, respectively.

Although we are only using a small number of layers, we can already observe from the transmission coefficient curves in Figures 22(a and b) how the band gap is formed. We show separately for each polarization the transmission coefficient curves for varying angles of incidence. The band gap location around 4000 nm is clearly identifiable for each curve. Further trends, which are visible in the band diagram of Figure 21, are identifiable in the transmission curve incidence-angle progression, such as gap widening, as well as a shifting of the stop-band center frequency.

One possibility for increasing the complete gap bandwidth is to create artificial stacks of photonic crystals, each with parameters tuned such that the crystal bandgap covers a region of the total bandgap. This may be designed by means of a numerical optimization, and will be the subject of a further investigation. Such a study would be useful to consider how fabrication inaccuracies may help increase bandwidth at the cost of decreasing the quality of the stop band.

For photonic crystal of the cubic symmetry we can write an equation of the Bloch amplitude as follows

$$\Delta E^{\tau}_{k,n}(\boldsymbol{r}) + \frac{1}{c^2}\omega_n^2(\boldsymbol{k})\varepsilon(\boldsymbol{r})E^{\tau}_{k,n}(\boldsymbol{r}) = 0 \tag{16}$$

Here $\omega_n(\boldsymbol{k})$ is the frequency of the n-th photonic band (Fig. 21). Bloch amplitudes can be normalized

$$\int_{\text{unit cell}} \varepsilon(\boldsymbol{r})E^{\tau *}_{k,n}(\boldsymbol{r})E^{\tau}_{k',n'}(\boldsymbol{r})\, d^3\boldsymbol{r} = M\delta_{n,n'}\delta_{\tau,\tau'}\delta_{k,k'}$$

where $M = 4\pi\hbar\omega_n(\boldsymbol{k})N_{\text{ph}}$, and N_{ph} is the number of photons in the unit cell.

Sometimes it is useful to consider propagation of light in a periodic photonic crystal as propagation of a quasiparticle where a free photon's frequency depends on its wave vector according to a sophisticated law. To do that, let us introduce the Wannier functions localized at the i-th site of the crystal

$$W^{\tau}_n(\boldsymbol{r}-\boldsymbol{R}_i) = \frac{1}{\sqrt{N}}\sum_k e^{-ik\boldsymbol{R}_i}E^{\tau}_{k,n}(\boldsymbol{r})$$

here N is the total number of "atoms" in the crystal, and we find the light field of the form

$$\boldsymbol{E}(\boldsymbol{r}) = \sum_{n,\boldsymbol{R}_i,\tau} E^{\tau}_n(\boldsymbol{R}_i)W^{\tau}_n(\boldsymbol{r}-\boldsymbol{R}_i)\boldsymbol{e}_{\tau},$$

Then for the envelope $E(\boldsymbol{R}_i)$ we obtain the equation

$$[\tilde{\Omega}_n(-i\nabla) - \omega^2]E^{\tau}_n(\boldsymbol{r}) - \frac{\omega^2}{c^2 M}\sum_{n',r'} E^{\tau}_{n'}(\boldsymbol{r})U_{n,n'}(\boldsymbol{r},\boldsymbol{r}') = 0 \tag{17}$$

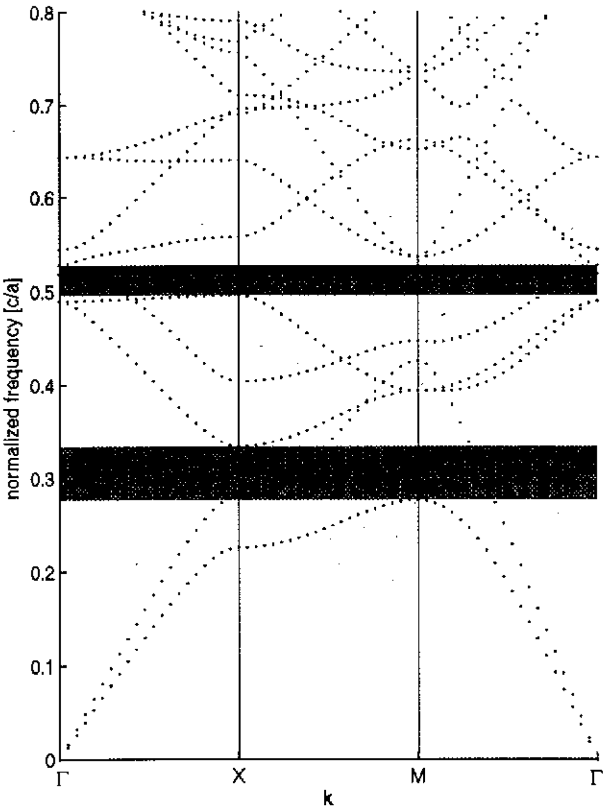

Fig. 21. Photonic band diagram for an infinite photonic crystal consisting of a square lattice of holes with radius 0.48 times the lattice constant, in a dielectric of relative permittivity 9. E_z and H_z modes are shown in blue and red dots, and E_z and H_z band gaps are shaded accordingly. An overlap in E_z and H_z band gaps produces the purple colored complete band gap near normalized frequency 0.5, corresponding to 4000 nm.

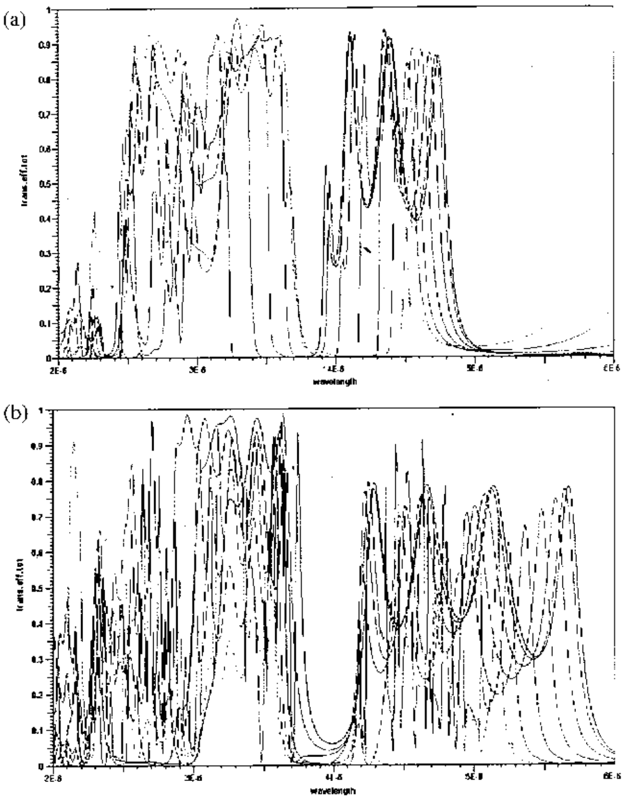

Fig. 22. Polarization transmission coefficient curves for the five-layer photonic crystal example. (a) E_z polarization. (b) H_z polarization. The darkest color corresponds to normal incidence, and the lightest color corresponds to an incidence of 80°. Very low transmission is apparent near the location of the idealized band gap.

where $\tilde{\Omega}_n(-i\nabla)$ is the Fourier transform of

$$\Omega_n(\boldsymbol{R}_i) = \frac{1}{N}\sum_{k}\omega^2_{k,n}e^{-ik\boldsymbol{R}_i}$$

i.e., $\omega^2_{k,n}$ after the substitution $\boldsymbol{k} \rightarrow -i\nabla$,

$$U_{n,n'}(\boldsymbol{r},\boldsymbol{r}') = \frac{1}{N}\int_V \delta\varepsilon(\boldsymbol{r})W^{\tau *}_{n'}(\boldsymbol{r}-\boldsymbol{R}_j)W^{\tau}_{n}(\boldsymbol{r}-\boldsymbol{R}_i)d^3\boldsymbol{r} \quad (18)$$

and $\delta\varepsilon(\boldsymbol{r})$ is a non-periodic addition to the dielectric permittivity caused by a defect, if it exists in the crystal.

In the absence of defects and apart from the photonic band gap we can assume $\omega_{k,n} = S_n\boldsymbol{k}$, where $S_n = c/\sqrt{\varepsilon_{\text{eff}}}$ is the effective speed of light in the i-th band. Then $\tilde{\Omega}_n(-i\nabla) = -S^2_n\Delta$, and the Eq. (17) reduces into the wave equation

$$\Delta E^{\tau}_n(\boldsymbol{r}) + \frac{\omega^2}{S^2_n}E^{\tau}_n(\boldsymbol{r}) = 0$$

the solution of which is the linear combination of plain waves $E^{\tau}_n(\boldsymbol{r}) = \exp(i(\omega/S_n)\boldsymbol{r})$.

By introducing the envelope function we substitute the problem of scattering and propagation of the Bloch waves in the photonic crystal with the simpler problem of scattering and propagation of the plane waves in the effective homogeneous space. Phenomenological parameters of this space (speed of light in the photonic bands as well as gap widths and positions) can be calculated after solving of Maxwell's equations in the perfect photonic crystal, as in Eq. (13). The effective potential of the defect Eq. (18) is usually localized in the vicinity of a lattice constant around $\delta\varepsilon(\boldsymbol{r})$. To obtain the actual electric field, and not its envelope, we multiply the envelope by the Bloch amplitude:

$$\boldsymbol{E}(\boldsymbol{r}) = \sum_{k,\tau}E^{\tau}_n(\boldsymbol{k})E^{\tau}_{k,n}(\boldsymbol{r})\boldsymbol{e}_{\tau}$$

To consider the problem of the light reflection/refraction at the boundary between the photonic crystal and a vacuum or between two photonic crystals, we have to impose the boundary conditions for the envelopes of the light fields. The simplest boundary conditions have been obtained in paper.[41] If we introduce the Cartesian coordinates with the z-axis directed along the normal to the boundary, then

$$[\boldsymbol{E}_x] = 0, \quad [\boldsymbol{E}_y] = 0$$

$$\left[\frac{\varepsilon\omega^2}{c^2q^2}\frac{\partial \boldsymbol{E}_{nx}}{\partial z}\right] + \frac{\omega^2}{c^2}\left(\alpha\boldsymbol{E}_{nx} + \sum_{n\neq n'}\beta_{n,n'}\boldsymbol{E}_{n'x}\right) = 0 \quad (19)$$

$$\left[\frac{\partial \boldsymbol{E}_{ny}}{\partial z}\right] + \frac{\omega^2}{c^2}\left(\alpha\boldsymbol{E}_{ny} + \sum_{n\neq n'}\beta_{n,n'}\boldsymbol{E}_{n'y}\right) = 0$$

Here the square brackets denote a discontinuity of the appropriate values at the boundary.

The envelope function approximation for the Maxwell equations has been suggested, and has been used to study the influence of point defects on the optical properties of PC,[42,43] optical properties of the photonic heterostructures,[44,45] and waveguides.[45,46]

5.1. Cylindrical Air Holes in Dielectric Media and Dielectric Rods Arrays

Ordered porous dielectric materials, for example air holes in a dielectric media or dielectric rods in air, are typical 2D photonic materials. To the best of our knowledge, silicon and alumina are the only materials, which could be obtained with extremely high pore quality, needed for photonic applications.[47] We will give two examples of obtaining porous alumina using anodic oxidation of aluminum. The ordering during anodic aluminum oxidation into arrays of the hexagonal openings was realized using preliminary spatial definition of the initiation sites (indentation).[48] Opening arrays of hexagonal, square, and triangular shapes were obtained as shown in Figure 23. Varying the opening size and interopening spacing in these structures can lead to photonic films with band gaps centered between 200 and 1300 nm. The arrays have high ordering quality, permitting their use as templates for the fabrication (filtration) of metal nanoparticles with well defined shape.

Two techniques were used for preparation of ordered pore arrays in anodic alumina.[49] In technique (1), as a result of a two-step anodization process, the ordered pore array was obtained with straight and ordered pores extending though the whole film as seen in Figure 24. The shown pore array can be characterized by pore diameter of 200 nm, uniform inter-pore distance of 460 nm and an aspect ratio of ~500. The main disadvantages of technique (1) (difficulty in controlling the self-organization stage of the process and multidomain film organization) were overcome by using technique (2), based on prepattern guided anodization. As a result, the hexagonal lattice of pores was obtained extending though the whole film.

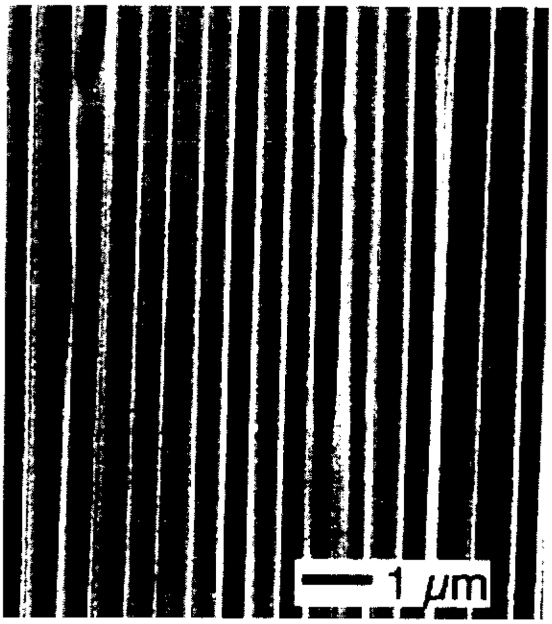

Fig. 24. Cross-section of the self-organized pore array in anodic alumina obtained using a two-step anodization process. Reprinted with permission from [49], A. P. Li et al., *Electrochem. Sol.-St. Letters* 3, 131 (**2000**). © 2000, ECS.

The monocrystalline pore arrangement can be seen from the FFT diagram, Figure 25.

Most dielectric rod two-dimensional photonic structures of high quality have been designed for optical communication using lithographic techniques, such as the rod array shown in Figure 26.[50–52] Among studies of materials with periodic refractive index, the two dimensional rod arrays in the self-organized composite crystals $Li_{1+x}Nb_{1-x}TiO_3$ should be mentioned, obtained by conventional floating zone melting crystal growth.[53] The crystallographic relation was found between the Li_2TiO_3 rods and $Li_{1+x}Nb_{1-x}Ti_xO_3$ matrix (phase M), as in Figure 27. To obtain this material, the mixture of Li_2CO_3, Nb_2O_5 and TiO_2 was isostatically pressed in a vacuum at 1120 °C for three hours. The crystal growth was carried out in a floating zone melting crystal growth system. In the obtained composite, the rod diameter is approximately 1 μm and

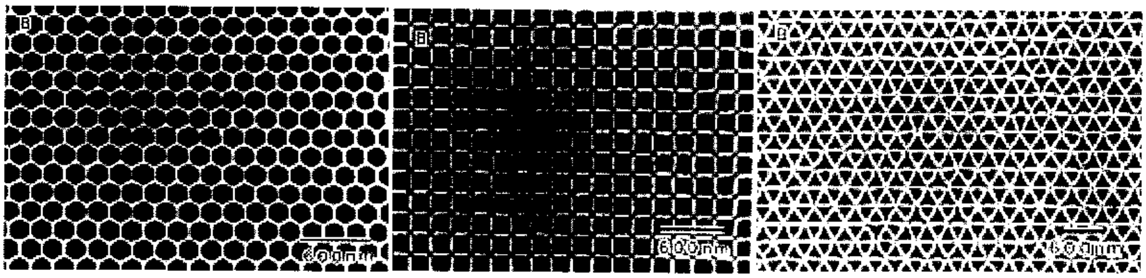

(a) (b) (c)

Fig. 23. 2D porous alumina photonic crystals, obtained by anodic oxidation of Al after spatial definition of the initiation sites. Openings have hexagonal (a), square (b), and triangular (c) arrangements. Bottom sides of the anodic alumina are shown. The scale bars of 600 nm are shown. Reprinted with permission from [48], H. Masuda et al., *Adv. Mater.* 13, 189 (**2001**). © 2001, Wiley Interscience.

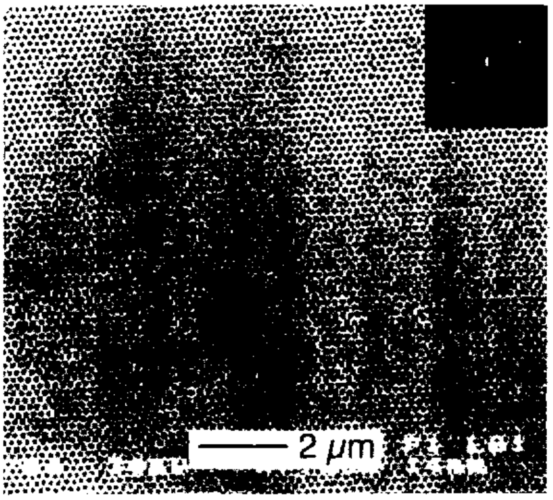

Fig. 25. Monocrystalline pore array in porous alumina obtained using prepattern guided anodization. Reprinted with permission from [49], A. P. Li et al., *Electrochem. Sol.-St. Letters* 3, 131 (**2000**). © 2000, ECS.

the distance between the rods is approximately 1–2 μm, the longitudinal direction of the rod-like precipitates corresponds to the perpendicular to the growth direction. Formation of unusual precipitate can be explained on the basis of a discontinuum precipitation mechanism (cellular precipitation), which can lead to the formation of a two-phase lamellar aggregate.

5.2. Enhancement of IR by Periodic Surface Modulation

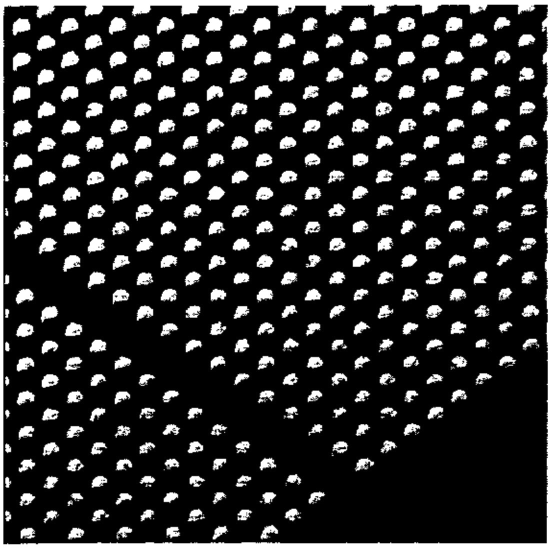

Fig. 26. Rod-type 2D photonic structure fabricated on a single crystal silicon wafer (~13 μm deep with 340 nm wide openings). The structure represents an integrated circuit waveguide with a smooth sidewall of aspect ratio of 50. Reprinted with permission from [50]. S. H. G. Teo et al., *Appl. Phys. A* 89, 417 (**2007**). © 2000, Springer.

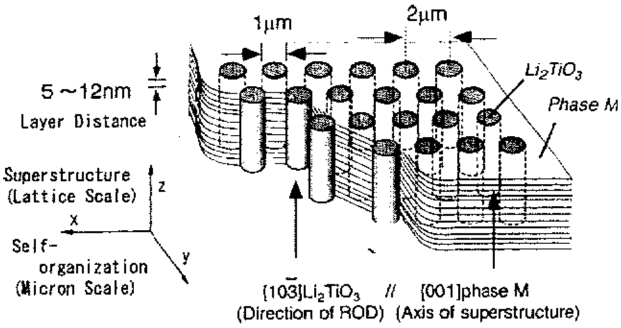

Fig. 27. Scheme of a self-organized microstructure in composite $Li_{1-x}Nb_{1-x}Ti_xO_3$. Reprinted with permission from [53]. Y. Yamamoto et al., *J. All. Comp.* 385, 252 (**2004**). © 2004, Elsevier.

Surface modification was shown to be one of the ways to enhance NWIR and MWIR.[54–56] These studies, which are results of merged photonic crystal and frequency selective surface approaches, design structures capable of emitting narrowband MWIR at high power with the bandwidth of light emitting diodes.[57]

It was shown that coherent IR sources over large distances in well defined directions can be fabricated using periodic microstructure in polar materials (SiC).[54] Such an antenna can radiate IR light in a narrow solid angle when it is heated. A dependence of emission spectrum on observation direction was also detected. This can be a

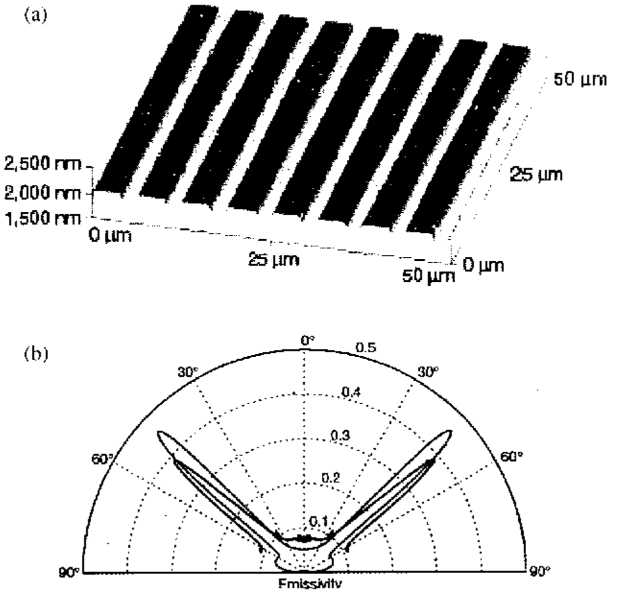

Fig. 28. Periodic surface used for the study of the enhancement of thermal sources by surface modification. (a) Grating on SiC substrate with period $d = 0.55\lambda$ ($\lambda = 11.36$ μm) and depth $h = \lambda/40$ fabricated by standard optical lithography. (b) Polar plot of the emissivity of the grating at $\lambda = 11.36$ μm for p-polarization. Experimental data are shown red, and calculations are green. The measurements are performed by recording the emitted intensity in the far field as a function of emission angle using an HgCdTe detector. The emission data were recorded for the sample in a local equilibrium at the temperature of 773 K. Reprinted with permission from [54], J.-J. Greffet et al., *Nature* 416, 61 (**2002**). © 2002, Nature.

consequence of the Wolf effect, or spatial correlation from random sources.[58, 59] The periodic structure producing a strong emissive peak around $\lambda = 11.36$ μm is shown on Figure 28(a), and the measurements of the thermal emission perpendicular to the line of the grating is shown in Figure 28(b). The explanation of how random thermal motion can generate a coherent current along the surface can be found in the coherent properties of surface waves such as surface-plasmon, polaritons or surface-phonon polaritons. Summarizing the results,[54] the modification of the surface profile can be used for tuning the direction and the intensity of the emissivity of the surface at a given wavelength, and for modification of the emission spectra in a given direction.

An interesting phenomena is the formation of a periodic self-assembled nanoporous network on the surface if the high-temperature ceramic is the composite $0.75(\mathrm{Zr_{0.88}Ce_{0.12}})\mathrm{O_2} - 0.25(\mathrm{La_{0.8}Sr_{0.2}})\mathrm{MnO_3}$, calcined at 1025 °C for 4 hours, and sintered at 1400 °C for 6 hours.[13] The resulting structure is shown in Figure 29. The pores have a diameter of 150–200 nm with a depth of the porous structure of 100 nm. In spite of the pore size being non-uniform, the pore distribution is quite periodic with the period of 50–150 nm. Appearance of the periodic surface structure is not a result of non-homogeneous constituent segregation, as was shown by magnetic measurements (the studied ceramic contained Mn). The phase-transformation-driven self-assembly to achieve minimum strain energy is the most probable explanation of the observed unusual phenomenon of surface periodic network formation.

5.3. Metal Thin-Film Periodic Hole Arrays

The coupling of the light into surface plasmon states can be used as an explanation of enhancement effects observed in metallic thin-film hole arrays. For example, the thermally-stimulated MWIR emitter was constructed, shown in Figure 30, which emits within a narrow band of $\delta\lambda/\lambda \leq 0.2$, and represent tetragonal hole arrays in silicon,[57] but similar results were obtained for arrays of different symmetries. The reflectivity dips were observed at a wavelength range of $\lambda \rightarrow a$. Generally, a linear relationship between the lattice parameter a and peak emission position was observed. The activation of surface-plasmon modes can explain the observed sharp emission properties. Of course the use of higher temperatures, which is necessary for higher power emission, will require high-temperature stable fabrication materials. The Transfer Matrix Method (TMM) was used for quantifying transmission and reflection properties of the fabricated devices.

The emissive properties of devices comprising thin Pt films on microstructured silicon profiles clearly indicated the presence of resonance between the emissive field and the microstructure, Figures 31 and 32.[5] Measurements of reflectance and emission spectra as well as rigorous coupled-wave analysis (RCWA) show that emission spectra depend on the period of the designed microstructure and can be used for the control of emission spectra.

The narrowband IR source is developed using a two dimensional metal-coated photonic lattice shown in Figure 33.[60] The absorption and emission (at 300–400 °C) were studied. The emission measurements revealed three stronger peaks at ~3.9, 4.17 μm (peaks at $\lambda < a$), and ~4.41 μm ($\lambda > a$) and two weaker peaks at ~3.81 and 4.92 μm, seen in Figure 34. The coupled surface-plasmon model and band structure calculation were performed in order to understand the physical reason of the observed emission spectra and to selectively excite them.

The capability of a narrow band thermal emission at a predicted wavelength was also demonstrated using a photonic device, shown in Figure 35, combining a silicon photonic crystal and sub-wavelength array of holes in a metal film with period a.[61] It is particularly remarkable that the array of metal holes on a uniform substrate does not produce resonant absorption or emission.

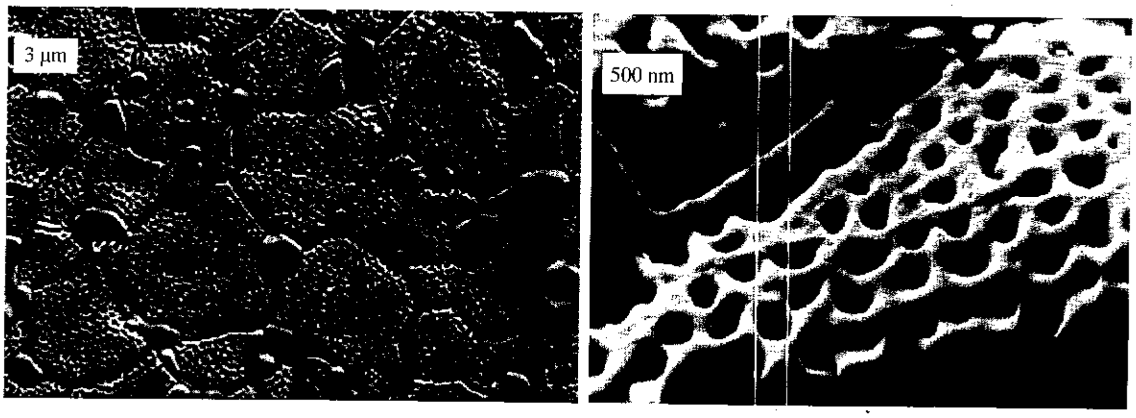

Fig. 29. Nanoporous periodic structure on the surface of composite $0.75(\mathrm{Zr_{0.88}Ce_{0.12}})\mathrm{O_2}$-$0.25(\mathrm{La_{0.8}Sr_{0.2}})\mathrm{MnO_3}$ ceramic. Reprinted with permission from [13], V. Sharma et al., *Appl. Phys. Lett.* 90, 123110 (**2007**). © 2007, American Institute of Physics.

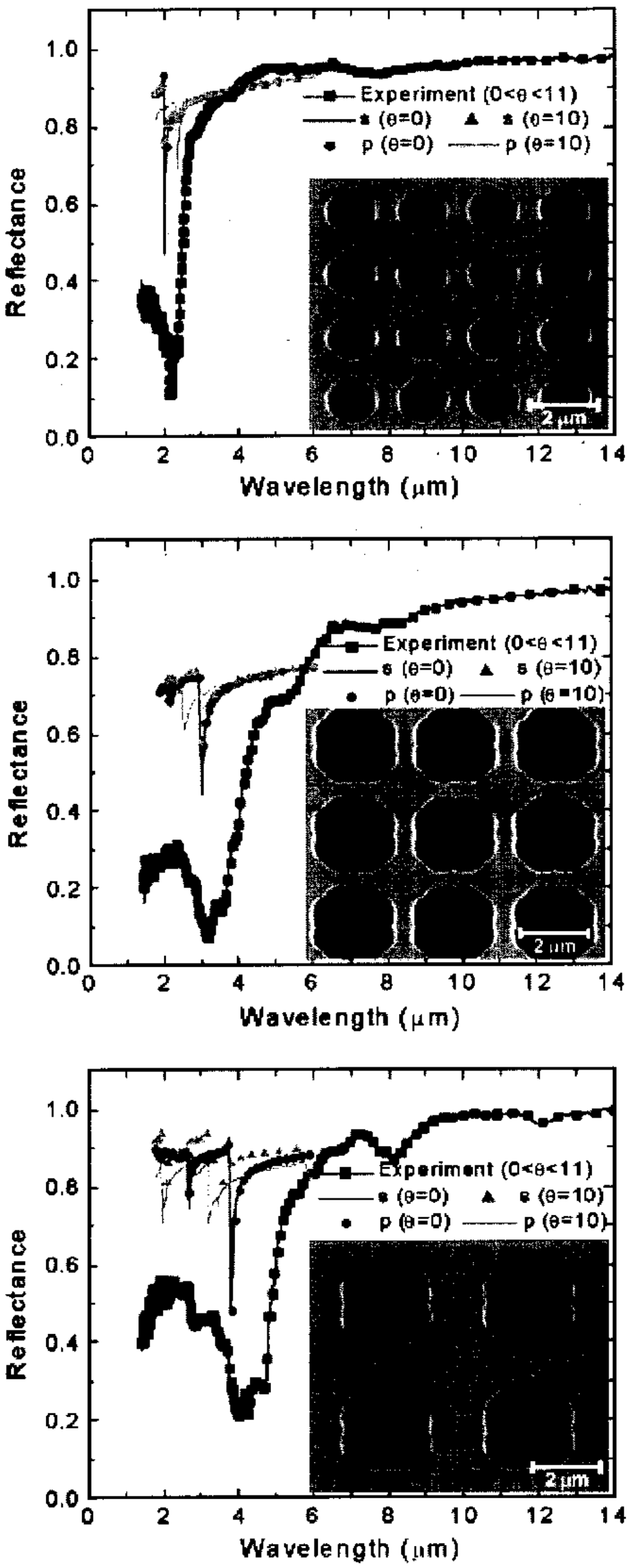

Fig. 30. Photonic devices with periods $a = 2, 3$, and 4 μm, fabricated using standard photolithographic technique and containing 0.15 μm thick deep reactive etched Au layers on Si. Reflectance, measured at room temperature, is shown. Reprinted with permission from [57], M. U. Pralle et al., *Appl. Phys. Lett.* 81, 4685 (**2002**). © 2002, American Institute of Physics.

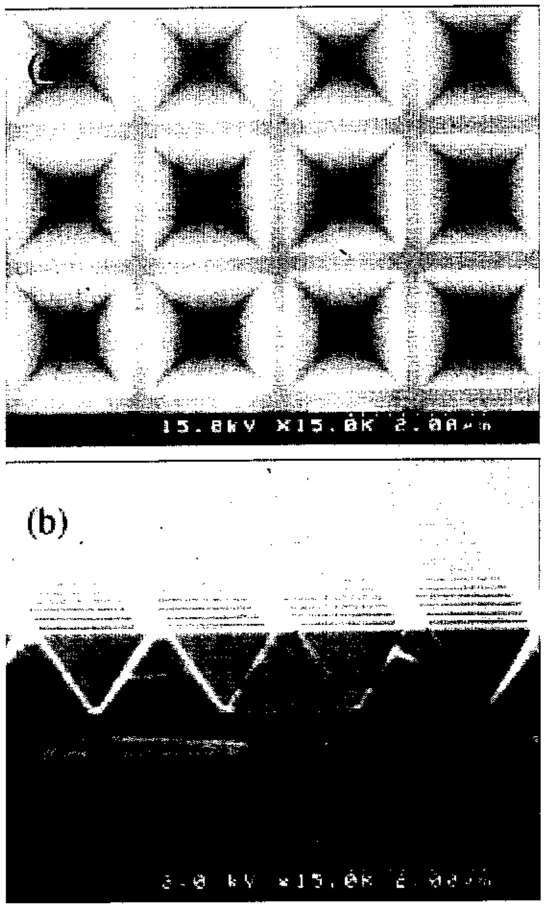

Fig. 31. Two dimensional periodic structure on a (100) Si wafer obtained by anisotropic etching and laser ablation. The whole structure, including parallel to substrate (100) surfaces and inclined pyramidal (111) surfaces are coated with ≈37 nm thick Pt layer. (a) Top view. (b) Cross-section view. Reprinted with permission from [5], H. Sai et al., *J. Opt. Soc. Amer. A* 18, 1471 (**2001**). © 2001, Optical Society of America.

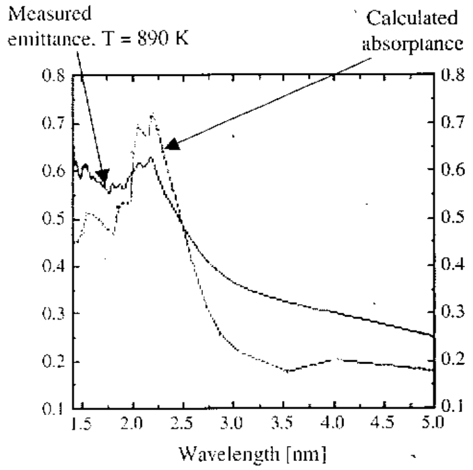

Fig. 32. Calculated and measured emittance spectra for structure with $a = 2.0$ μm. The spectrum was measured with a triglycine sulphate detector in normal mode. Absorbance spectrum was calculated for $\Theta_i = 5°$ (incidence angle) and $\psi_i = 45°$ (polarization angle). Reprinted with permission from [5], H. Sai et al., *J. Opt. Soc. Amer. A* 18, 1471 (**2001**). © 2001, Optical Society of America.

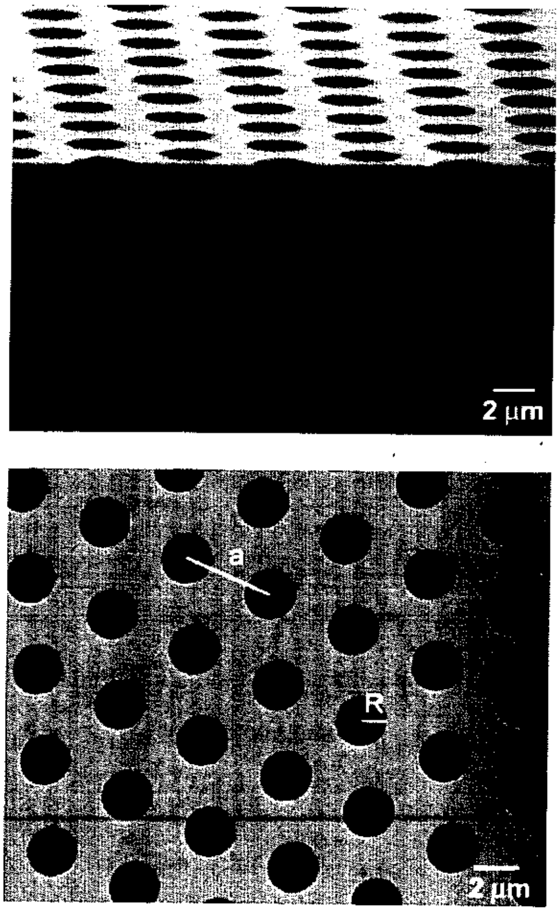

Fig. 33. Two dimensional metallo-dielectric photonic crystal formed by a hexagonal lattice of circular holes. A thin 100 nm Pt film was deposited using e-beam evaporation onto the n-doped Si wafer. The array of air holes has been etched through the metal layer. Period a is 4.2 μm, hole radius R is 1.05 μm, and total depth of air holes is 8 μm. Reprinted with permission from [60], I. Puscasu et al., *J. Appl. Phys.* 98, 013531 **(2005)**. © 2005, American Institute of Physics.

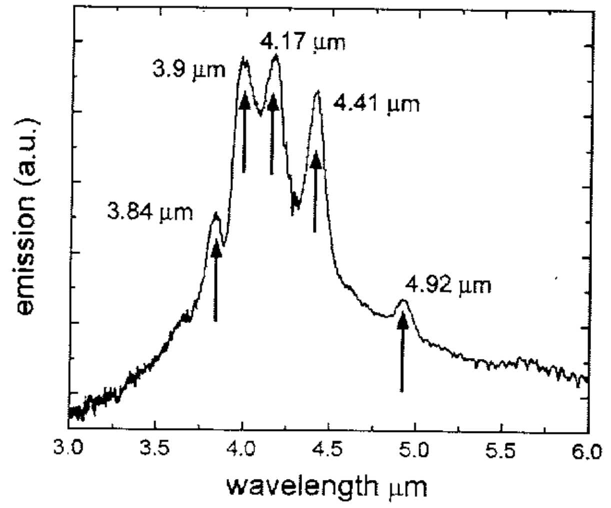

Fig. 34. Emission spectra from the hexagonal lattice structure shown in Figure 25. Reprinted with permission from [60], I. Puscasu et al., *J. Appl. Phys.* 98, 013531 **(2005)**. © 2005, American Institute of Physics.

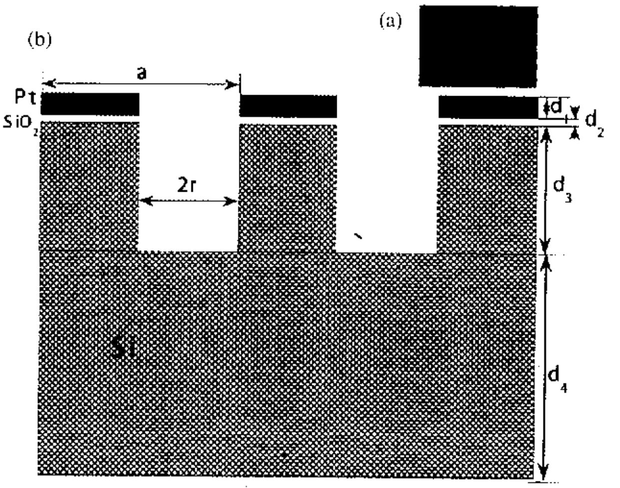

Fig. 35. Emitter, consisting of a metal hole array and a silicon photonic crystal. Device was fabricated using standard photolithography and deep reactive ion-beam etching. (a) Top view showing hexagonal structure of the hole array. (b) Cross-section. Pt film is green, silicon photonic crystal is grey, $a = 4.2$ μm (photonic structures with $a = 3.4$–6.2 μm produced similar results), $r = 0.25$, $a = 1.05$ μm, $d_1 \approx 0.1$ μm, etching depth d_3 was varied, $d_4 = 372$ μm. Intermediate SiO_2 layer with thickness $d_2 = 0.1$ μm was deposited between Pt and Si layers. Reprinted with permission from [61], R. Biswas et al., *Phys. Rev. B* 74, 045107 **(2006)**. © 2006, The American Physical Society.

6. 3D HIGH-TEMPERATURE PHOTONIC STRUCTURES

The theory of the black body heat radiation is based on linear dependence between the photon frequency and wave vector

$$\omega = ck = 2\pi c/\lambda \tag{20}$$

Assuming that photons are placed in a cube of dimension $L_x \times L_y \times L_z$ and using the Gibbs distribution of the photon energies $\hbar\omega(k)$, we can obtain Plank's law (2). Actually, this is the density of photonic states for the linear dispersion law (20). This law does not hold in photonic crystals and, therefore, Plank's law has to be modified.

The explanation is simple. All the radiation falling on the crystal is absorbed there, and then reemitted according to the photonic band spectrum. The spectrum of the photonic crystal contains gaps, and radiation is significantly modified in the proximity of them. As a result, the peaks of radiation should be expected at the peaks of the density of photonic states, which are usually close to the band edges. Indeed, $\partial\omega/\partial k = 0$ at the band edges; this means that the $\omega(k)$ curve has a zero slope there. The longer the horizontal part of the curve, the larger the corresponding peak in the photonic density of states.

The effect is not appreciable in free space, where the horizontal part in the curve is absent. There are two cases that have to be considered in particular. First, we consider photonic crystals composed of dielectrics with large dielectric permittivity. In this case the effect is due to the flattening of the band spectrum in the vicinity of the gap

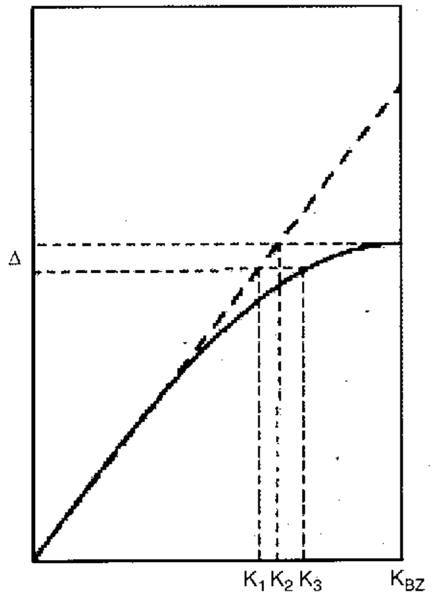

Fig. 36. Lower bands of a photonic crystal (bold blue curve) and a bare material (dashed red curve). k_{BZ} is the wave vector corresponding the edge of the Brillouin zone. The differences $(k_{BZ}-k_3)$ and (k_2-k_1) are proportional to the number of photonic states it the frequency interval Δ.

considered above. Figure 36 schematically demonstrates the effect. The number of photonic states in some interval Δ is proportional to the corresponding interval of the wave vectors. This interval for the photonic crystal $k_{BZ}-k_3$ is larger than that for the bare material k_2-k_1.

This effect has been observed in the experiments on the three-dimensional photonic crystal fabricated of silicon rods and having diamond symmetry.[62] In Figure 37, we see an increase of the infrared emission for the frequencies below the gap, and a decrease in the gap region. In a second example, the photonic crystals could be composed of metals, whose dielectric permittivity is either negative [$\varepsilon=-24.8+0.8i$ (Au), $\varepsilon=-33.5+3.1i$ (Ag)], imaginary [$\varepsilon=4.3+19.4i$ (W)] or both [$\varepsilon=-22.5+22.7i$ (Pd)].[a] If the metal occupies a significant part of the crystal, the effective dielectric permittivity of the photonic crystal (32) is also negative or imaginary. This means that the low frequency long wavelength photons can't propagate through this crystal, and only the photons, whose frequency is close to the gap, can spread. The wavelength of such photons is comparable with the crystal lattice constant.

To understand propagation of short wavelength photons in the metallic photonic crystal, we begin with a photon localized in a unit cell. Its localization is due to reflection from each side of the metal rods surrounding the cell. This localization would be perfect, if the rods were infinitely thick. Finiteness of the rod thickness allows the photon wave field to penetrate into neighboring cells. Such "tunneling" explains the light wave propagation in second type photonic crystals.

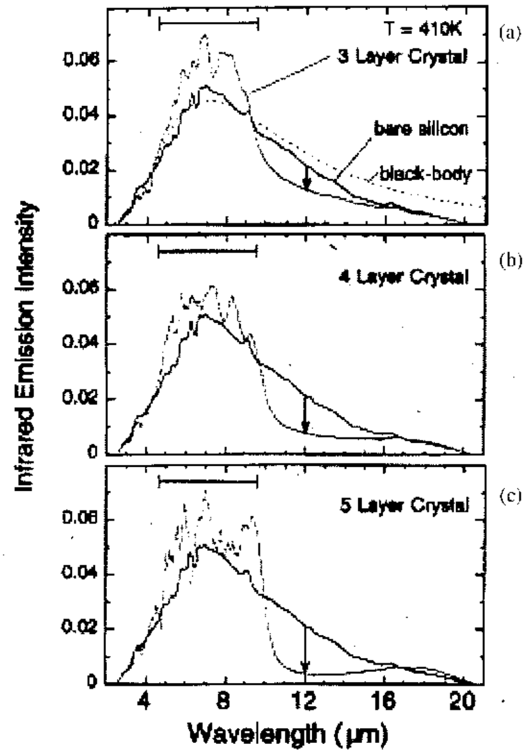

Fig. 37. Measured thermal emission spectra of a three dimensional silicon photonic crystal of different numbers of layers ($n=3$, 4, and 5). Solid black and dashed lines correspond to the theoretical bare silicon and black-body emission spectra, respectively. Reprinted with permission from [62], S.-Y. Lin et al., *Phys. Rev. B* 62, R2243 (**2000**). © 2000, The American Physical Society.

Consider light propagation in a one dimensional metallic photonic crystal. This could also be a two or three dimensional cubic photonic crystal, if light propagates along the [1 0 0] direction. The photonic spectrum of this crystal obeys Eq. (9), where $\varepsilon_1=1$ and ε_2 is the dielectric constant of the metal, $\sqrt{\varepsilon_2}=n_0+ik_0$, d_1 is the thicknesses of the metal rod, and $l=d_1+d_2$ is the unit cell. Assuming the thicknesses of the metal rod to be large, $\exp(\omega k_0 d_2/c)\gg 1$, and $|\varepsilon_2|\gg 1$, we can rewrite Eq. (9) as

$$2\cos kl=\left(\cos k_1d_1+\frac{n_0+ik_0}{2i}\sin k_1d_1\right)e^{-i\omega n_0 d_2/c+\omega k_0 d_2/c} \tag{21}$$

In this equation $k_0\exp(\omega k_0 d_2/c)\gg 1$, which means the value of k is real, if $\sin k_1d_1\ll 1$. In the zero approximation $\sin k_1d_1=0$; this corresponds to the light localization mentioned above.

The solution of Eq. (21) can be real only if $n_0=0$. This means that ε_2 is real, but negative. Therefore, the reflection of light on the metal surface occurs without

---

[a] The data correspond to a photon energy of 1.5 eV or a wavelength of $\lambda=0.827$ μm in vacuum.

its absorption. Otherwise, the light wave would attenuate, because of energy dissipation due to Joule heating. Assuming $n_0 = 0$, we can write the solution of Eq. (21) as

$$\frac{\omega}{c} = \frac{\pi N}{d_1} - \frac{2}{k_0 d_1} + (-1)^N t \cos kl \tag{22}$$

where $N = 1, 2, 3, \ldots$ (we assume $N \neq 0$ to make the frequency (22) positive),

$$t = \frac{4}{k_0 d_1} e^{-(\pi k_0 d_2/d_1)N}$$

is a hopping parameter ($t \ll \pi/d_1$, $d_2 \ll d_1$). The dispersion relation (22) is typical for a tight binding model of the electron band structure.

In general, the solution of Eq. (21) is

$$\frac{\omega}{c} = \frac{\pi N}{d_1} - \frac{2}{(k_0 - in_0)d_1} + (-1)^N \frac{k_0}{k_0 - in_0} \eta t \cos kl,$$
$$\text{where } \eta = e^{i\omega n_0 d_2/c} \approx e^{(i\pi n_0 d_2/d_1)N} \tag{23}$$

The assumption $n_0 \ll k_0$ is characteristic of the good conductors: gold, silver, and copper. For most of metals these values are of the same order $n_0 \sim k_0$. Solutions ω of Eq. (21) for real k (in the infinite crystal) are complex. This corresponds to a broadening of the spectrum. Moreover, broadening of the non-physical solution $N = 0$ in Eq. (22) $\omega = -2c/k_0 d_1$, if it exceeds this value, could appear in the appropriate density of the photonic states.

Emission spectra of the tungsten photonic crystals have been investigated theoretically by El-Kady et al.[63] Figure 38(a) presents a band spectrum of the tungsten Lincoln-log photonic crystal. We see that the first photonic band of the crystal starts with a nonzero frequency. As a result, the density of the photonic states and emission spectrum contain only two peaks around the band edges, as seen in Figures 38 and 39.

The wings in the experimental curves are probably due to a broadening of the photonic spectra mentioned above (for tungsten $n_0 = 3.48$, $k_0 = 2.79$ for $\lambda = 0.827$ μm in vacuum). Moreover, they could arise from surface photonic states. Such states with complex wave vector have to exist at the photonic crystal boundary and participate in photon emission. These states have not been taken into account in the modeling. Another possible reason for the broadening is tails of the photonic states in the gap arising in imperfect photonic crystals.

6.1. Tungsten Emitters in Near- and Mid-Infrared for Thermal Photovoltaic Power Generation

On of the aims of application of photonics in photovoltaics (TPV) is to suppress radiation below the band gap E_g. This can be accomplished by the construction of refractory metals with an electrically heated photonic structure enhancing radiation within distinct a photonic band. The emitters for

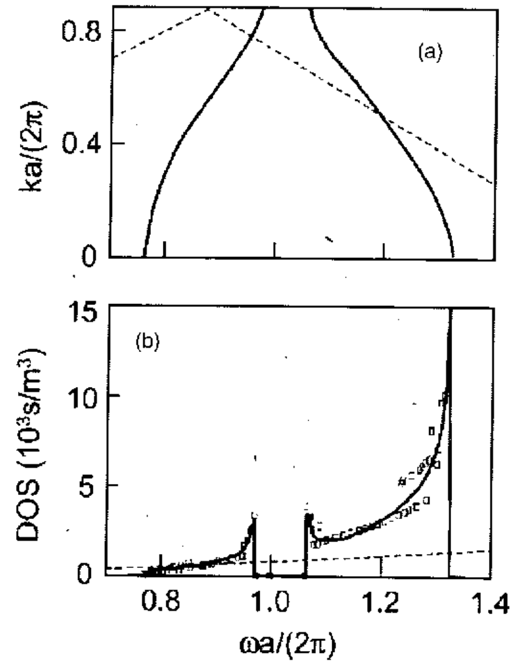

Fig. 38. (a) Calculated photonic spectra of free space (dashed line) and photonic crystal (solid line). (b) Calculated density of states of free space (dashed line) and photonic crystal (dots); the solid line is the least-squares fit to the dots. Reprinted with permission from [63], I. El-Kady et al., *Phys. Rev. B* 72, 195110 (**2005**). © 2005, The American Physical Society.

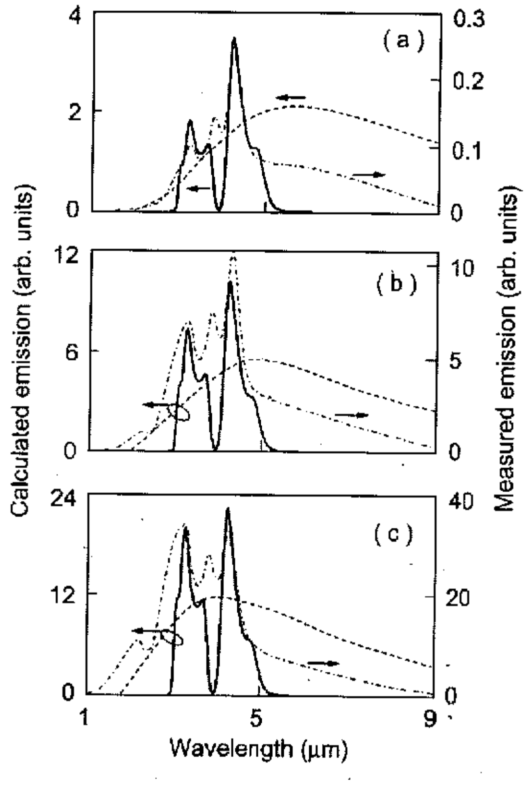

Fig. 39. Calculated black body emission spectra of free space (dashed line) and photonic crystal (solid line) for $T = 500$ K (a), $T = 600$ K (b), and $T = 700$ K (c). Dash-dotted lines are the experimental spectra. Reprinted with permission from [63], I. El-Kady et al., *Phys. Rev. B* 72, 195110 (**2005**). © 2005, The American Physical Society.

incandescent lamps, based on photonic tungsten structures are also patented.[64]

In order to achieve this objective, the 3D tungsten photonic crystals with a complete photonic band gap at different wavelengths have been fabricated. The photonic crystal shown in Figure 40(a) suppresses photonic emission at $\lambda > 3$ μm (photonic band gap) and shows the peak at $\lambda \approx 1.5$ μm (SWIR range) within a narrow spectral band of $\Delta\lambda \approx 0.9$ μm at the temperature of $T \approx 1535$.[65] The calculated absorption spectrum shows low absorption for $\lambda > 3$ μm, and two peaks of $\approx$40% at $\lambda \approx 2.5$ μm and of $\approx$80% (high plateau) at $\lambda \approx 1.5$–1.9 μm in Figure 40(b). This fabricated photonic tungsten emitter has a complete photonic band gap and can trap the light in all directions for both polarizations. The measured photonic emission is 2.5 times narrower than blackbody radiation at $T \approx 1500$ K and has its peak at the lower wavelength of $\lambda \approx 1.5$ μm, Figure 41. The estimated optical-to-electric conversion efficiency of the suggested three dimensional photonic tungsten emitter is $\eta \approx 34\%$, and electric power density $\approx$14 W/cm^2 at $T \approx 1535$ K, which exceed the efficiency of power of conventional emitters (blackbody, structured tungsten, Eu_2O_3).[65] As indicated in paper,[66] the designed tungsten photonic emitter is capable of providing nearly two hundred times stronger peak power of 40 W cm^{-2} μm^{-1} at $\lambda \approx 1.5$ μm at $T \approx 1500$ K than the peak power of 0.2 W cm^{-2} μm^{-1} at $\lambda \approx 450$ nm of solar radiation reaching the earth. At the same time, subsequent experiments show,[67] that the temperature distribution takes place in the electrically heated tungsten photonic samples and a relatively small variation in temperature can lead to large changes in the emission intensity.

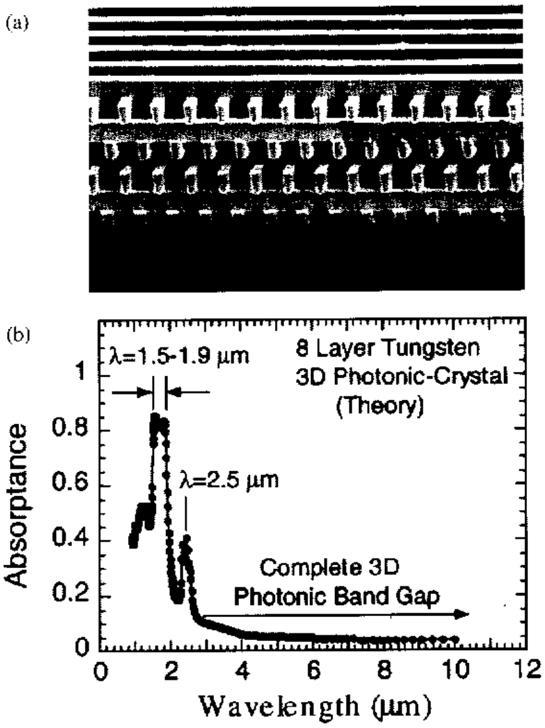

Fig. 40. Three dimensional tungsten photonic emitter designed using modified silicon technology. (a) SEM pattern. Separation rod has a = 1.5 μm, rod width $w = 0.5$ μm, and rod height ≈ 0.75 μm. Tungsten rods represent the 110 chains of a diamond lattice. (b) Calculated absorption spectrum of 8-layered 3D tungsten photonic crystal. Reprinted with permission from [65], S. Y. Lin et al., *Appl. Phys. Lett.* 83, 380 (**2003**). © 2003, American Institute of Physics.

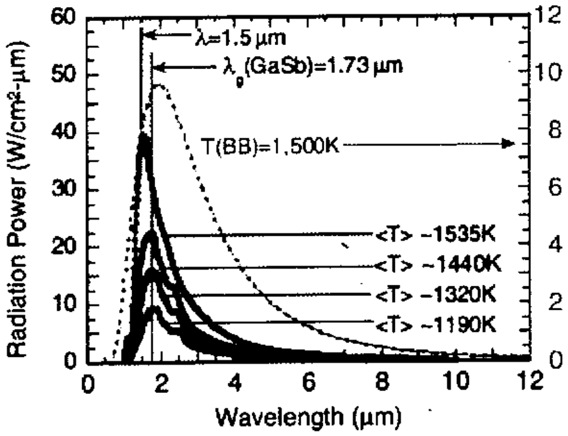

Fig. 41. Comparison of measured emission power of the tungsten photonic emitter from Figure 40 at effective temperatures of 1190, 1320, 1440, and 1535 K with blackbody radiation (dotted line). The GaSb band gap position is also shown. Reprinted with permission from [65], S. Y. Lin et al., *Appl. Phys. Lett.* 83, 380 (**2003**). © 2003, American Institute of Physics.

Using the same microlithography process, tungsten lattices with complete photonic band gaps at broader wavelengths are also feasible. The tungsten photonic lattices with photonic band gap λ between 3 and 20 μm (MWIR, LWIR and Far-IR) are reported.[4,68,69] The structures possess very strong attenuation of $\approx$30 dB at 12 μm, a sharp absorption peak at the photonic edge, and very high transmission in the allowed band.[69] The dominance of light emission in a narrow band at a constant energy conversion was underlined.[68]

Notice that TPV cells can efficiently operate independently on weather conditions and can be considered as a complimentary technology to solar energy.[65]

6.2. Organized Fiber Structures

Depending on the high-temperature stable fiber properties, different methods can be used for fiber organization in HTPS. As the simplest way, methods of self-assembling can be considered. Self-assembly was used for the organization of inorganic fibers at high temperature, for example of transition metal inorganic nanotubes.[70] The structurally well-organized fiber mats of SCS-6 silicon carbide fibers were produced using High Isostatic Pressure (HIP) consolidation at 116 MPa.[71]

Fabrication of woven structures is also a possibility to obtain two- or three-dimensional photonic structures, as an alternative to lithography methods. Materials made of

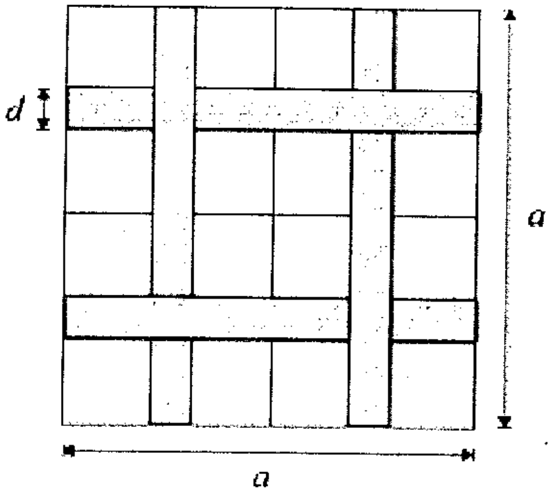

Fig. 42. Top view of a rectangular woven structure. Reprinted with permission from [18], Y.-C. Tsai et al., *J. Phys.: Condens. Matter* 10, 753 (**1998**). © 1998, Institute of Physics.

fibers woven into 3D structure with micrometer cross-sections can possess full three-dimensional photonic band gaps in the mid-IR range, which allows woven structures to suppress electromagnetic waves in any direction.[72] For example, rectangular woven structures such as the one in Figure 42 can be fabricated, having the full 3D photonic band gap in mid-IR and working as photonic insulator, provided the lattice parameters (fiber size) can be adjusted to match the incident wavelength and that fiber with suitable dielectric constants can be found.

In the course of modeling properties of fiber assemblies, the randomly homogeneous model structure with orthogonally arranged fibers in Figure 43 was considered and the calculation of the influence of high-temperature elongation of fiber structure TC (see also Section 2.1) was performed for the fiber quartz ceramic structures (for example via the change of fiber length, fiber diameter). This model can be used for estimation of the radiative conductivity of imperfect fibrous composites.[22]

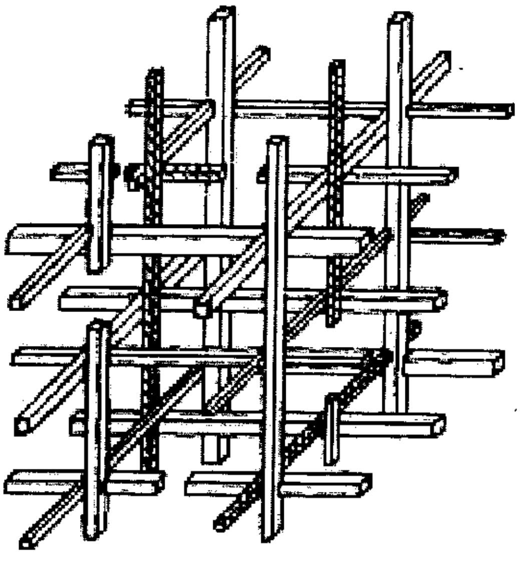

Fig. 43. Randomly homogeneous fibrous structure with orthogonally arranged fibers used for modeling the influence of high-temperature on the TC of fiber composites. Reprinted with permission from [22], N. A. Bozhkov and A. A. Ivanov, *J. Eng. Phys.* 541 (**1990**). Translated from *Inzhenerno-Fizicheskii Zhurnal* 58, 714 (**1990**). © 1990, Plenum Publishing Corporation.

The main high-temperature characteristics which are practically important for fibers and fiber-forming materials are the relaxation and phase transition temperatures in the amorphous regions (know as the glass point T_g), crystalline structural regions (the melting point T_m), and the upper temperature level of thermal stability, which is determined by the nominal decomposition temperature T_d. Inorganic fibers based on SiC, BN, AlN, SiO_2, Al_2O_3, and ZrO_2 have high resistance to heat and fire and can used at temperatures of 800–1000 °C, and briefly even up to 1500–2000 °C. The melting point of these inorganic fibers is within the range of 1700–2800 °C.[73]

7. PROPAGATION OF ELECTROMAGNETIC WAVES IN IMPERFECT PHOTONIC MATERIALS

There are two basic types of unintentional imperfection defects in photonic crystals. First, long range distortions in the lattice constant arise due to a variation in the sizes of the units composing the crystal. In the closely packed lattices this leads to an appreciable deviation of the lattice constant over long distances, depicted in Figure 44(a). Another reason for a long-range distortion can arise from the polycrystalline nature of a real crystal.[74,75] Second, imperfections may arise due to point defects, such as the presence of foreign particles of different dielectric constants, depicted in Figure 44(b).

Structural defects lead to a scattering of the electromagnetic Bloch wave, as has been observed in number of experiments. Figure 45 presents the transmission spectra of a opal photonic crystal built of silica particles as well as results of modeling based on the photonic band calculation for the corresponding perfect crystal.[74] We see that

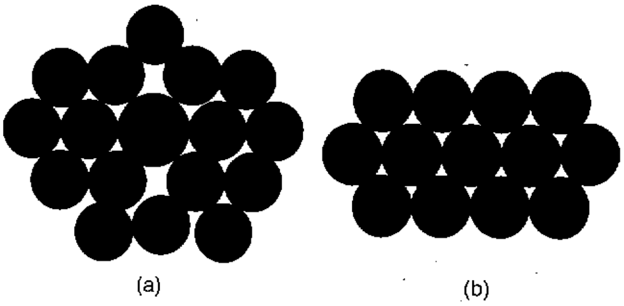
(a) (b)

Fig. 44. Schemes illustrating models of long- and short-range imperfections in photonic crystals. (a) Long-range distortion of the crystal lattice caused by impurity of different size. (b) Short-range distortion of the crystal lattice caused by impurity of different dielectric permittivity.

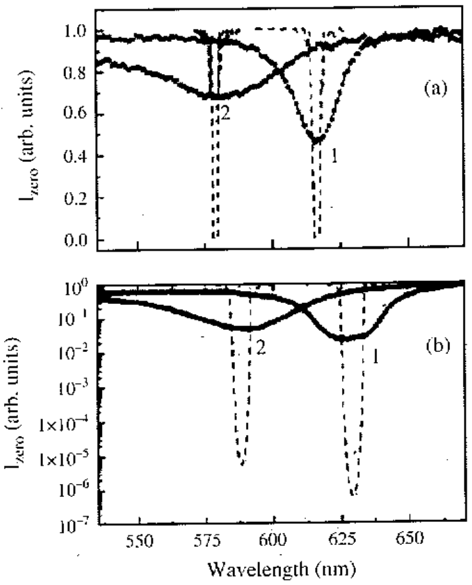

Fig. 45. Experimental (solid lines) and theoretical (dashed lines) zero-order transmission spectra (a) for infiltration with ethanol and (b) with cyclohexane. The spectra marked 1 represent normal incidence (u50°), while the spectra marked 2 show the case of incidence at u530°. The calculations predict significantly stronger attenuation and narrower spectral width of stop band features even though the calculated thickness of the structure was smaller @90 mm, corresponding to 384 close-packed (111) layers with interplane spacing of d5233 nm# than the actual thickness of the sample (D5300 mm). Reprinted with permission from [74], V. N. Astratov et al., *Phys. Rev. B* 66, 165215 (**2002**). © 2002, American Physical Society.

experimental dip is wider and shallower than the theoretical dip of the perfect crystal. A similar result has been obtained in another study, shown in Figure 46.[76] The one dimensional model of the structure disorder used in this paper makes the results more realistic, but does not go far enough to explain the demonstrated effect.

This effect has been explained to be a result of Bloch wave scattering at defects.[77] A widening of the transmittance curve can be understood as the result of light wave interaction with a long-scale distortion. Such distortion effectively changes the lattice constant and shifts the gap center frequency, making it position-dependent. As a result, photons with perfect crystal gap frequency can propagate without attenuation in some regions of the imperfect crystal where the gap position is different. On the other hand, some photons with frequency outside the perfect crystal gap may propagate with attenuation in some regions of the imperfect crystal. Thus, the long-range irregularities should lead to a widening of the dip in the transmittance spectrum, and an increase of the in-gap transmittance.

Light propagation in structures with long-range irregularities can be described by a wave equation with a position dependent effective speed of light S. As a result the width of the photonic band also becomes position dependent. We can write this dependence as $W = W_0(1+\beta\delta f)$,

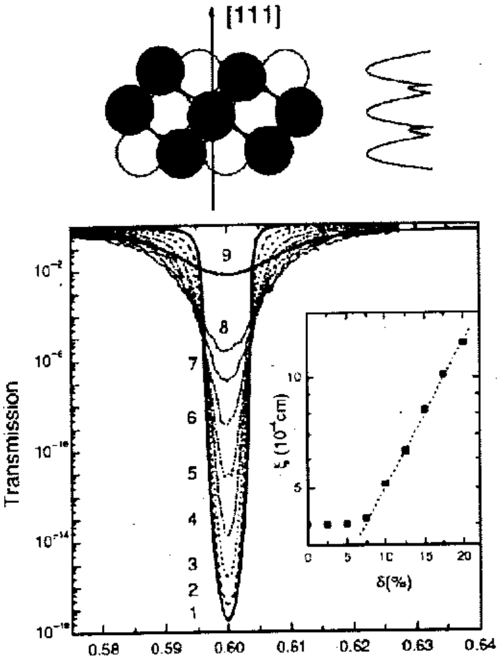

Fig. 46. Calculated transmission spectra for a photonic crystal of 165-mm thickness with varying disorder, each ensemble averaged over 200 realizations. The standard deviation d of the sphere diameter is 1–0%, 2–0.5%, 3–1%, 4–2%, 5–3%, 6–4%, 7–5%, 8–10%. Thick solid line 9 is the experimental spectrum. Upper inset: Scheme of sphere packaging on the (1 1 0) plane of an fcc lattice of opal, and corresponding profile of refractive index calculated along the @111# direction. Lower inset: A semilogarithmic plot of calculated attenuation length j as a function of disorder d. Reprinted with permission from [76], Yu. A. Vlasov et al., *Phys. Rev. B* 60, 1555 (**1999**). © 1999, American Physical Society.

where W_0 is the bandwidth of the perfect crystal, δf is local deviation of the packing density, and $\beta \sim 1$ is constant. Assuming a normal distribution of the random value δf, we can write the transmission as[77]

$$J_{\text{LR}} = e^{-4\alpha d},\ \text{where}\ \alpha = \frac{1}{\sigma\sqrt{2\pi}}\int_{-\infty}^{+\infty} e^{-\xi^2/2\sigma^2}\sqrt{\gamma+\xi}\,d\xi,$$
$$\gamma = \frac{(\omega^2-W^2)^2 - W^2\Delta^2}{4S^2\Delta^2}; \qquad (24)$$
$$\text{and}\quad \sigma^2 = \frac{(\omega^2 - W_0^2 + \Delta^2/2)^2}{S^4}\beta^2\langle\delta f^2\rangle$$

Rough simplification of Eq. (24) yields

$$J_{\text{LR}} \sim e^{-4\Delta/S(1-\beta^2\delta f^2)d} \qquad (25)$$

for the mid-gap transmittance, and

$$\sqrt{\delta\lambda_{\min}^2} \cong \beta\lambda_{\min}\sqrt{\delta f^2} \qquad (26)$$

for width of the dip.

Thus, long-scale irregularity leads to widening of the curve and some decrease of its depth. An additional

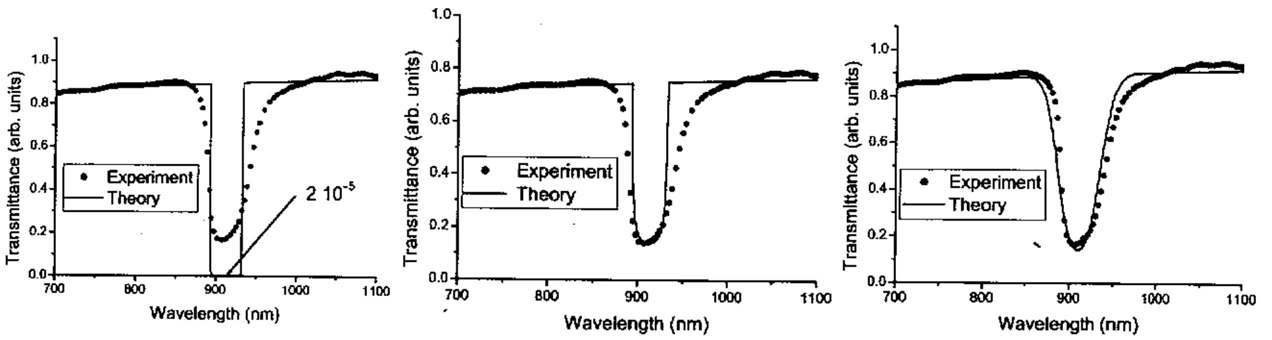

(a) (b) (c)

Fig. 47. Transparency of a photonic crystal under normal incidence. (a) The theoretical curve corresponds to the model of the perfect crystal. (b) The theoretical curve corresponds to the model of short-range irregularity. (c) The theoretical curve corresponds to the model of the long-range irregularity. Reprinted with permission from [77], L. Braginsky and V. Shklover, *Phys. Rev. B* 73, 085107 **(2006)**. © 2006, The American Physical Society.

decrease of the dip can arise from scattering due to short-scale irregularity in the pseudo-PBG photonic crystal. The position of the mid-gap is determined by the edge of the Brillouin zone, and therefore depends on the propagation direction in the crystal. The gap width is small in photonic crystals of low index materials. The gap is not absolute in such materials and propagation may be prohibited in some directions, but possible at the same frequency for other directions.

If the frequency ω belongs to the photonic gap in the direction of the normal $\boldsymbol{n}$ to the crystal boundary at $z = 0$, then propagation in this direction is prohibited. However, mid-gap position depends on direction in the crystal, and if the gap value is small, then the same ω can be outside the gap in some direction close to $\boldsymbol{n}$. If so, then elastic scattering of light can increase the in-gap transmittance. Thus, transmittance of a thick film depends on the number of scatterers along the decay direction, and not on the film thickness itself. Estimation yields

$$J_{\mathrm{SR}} = \frac{1}{\gamma L_i} \ln\left(\frac{\omega}{\Delta}\right)(1 - e^{-4\gamma d}) \tag{27}$$

where L_i is the mean free path of the photon regarding to its scattering at the impurities [41]. It can be estimated that

$$L_i = \frac{2S}{J_{\min}\Delta} \ln \frac{W}{\Delta} \tag{28}$$

Figure 47 illustrates the effect of structure distortion. The value of the band gap used in the theoretical model was chosen from the experiment. The theoretical midgap transmittance is four orders of magnitude smaller than the measured transmittance, Figure 47(a). Figure 47(b) demonstrates the effect of short-range irregularities. Such irregularities can increase the midgap transparency, but cannot cause broadening of the dip. Short-range scattering changes the wave vector of the in-gap photon such that it is no longer in-gap. The inverse process is improbable in narrow-gap photonic crystals. The effect of long-range irregularities is demonstrated in Figure 47(c). In agreement with approximations (25) and (26), the long-range irregularity causes a broadening of the gap.

8. PROPAGATION OF ELECTROMAGNETIC WAVES IN NON-ORGANIZED NANO- AND MICROGRANULAR MATERIALS

According to the approximation in (7), most of the thermal radiation energy at $T > 1000$ °C is transferred by IR radiation with wavelength $5\ \mu\mathrm{m} < \lambda < 20\ \mu\mathrm{m}$. These wavelengths are very large in comparison with the average grain size in some ceramics ($d \sim 100$ to 500 nm). However, they are smaller than or roughly equal to the average pore size in some porous materials ($d \sim 1$ to 50 μm). To investigate propagation of waves in such materials, we have to consider both limiting cases; materials with small-scale irregularity (e.g., grains of $d \ll \lambda$) and materials with large-scale irregularity (e.g., pores of $d \gg \lambda$). The first case will be addressed in this section.

Consider propagation in a granular material assuming that the mean size of grains is much less than the wavelength λ and that the material has no periodic organization with a period comparable to λ. The first assumption allows averaging of the electric and magnetic field deviations caused by structural disorder over the scale of the wavelength.

Suppose we have a dielectric function

$$\varepsilon(\boldsymbol{r}) = \begin{cases} \varepsilon_1, & \text{if } \boldsymbol{r} \text{ belongs to the grain} \\ \varepsilon_2, & \text{if } \boldsymbol{r} \text{ belongs to the surrounding material} \end{cases} \tag{29}$$

We can write $\varepsilon(\boldsymbol{r}) = \varepsilon + \xi(\boldsymbol{r})$, where $\varepsilon = p\varepsilon_1 + (1-p)\varepsilon_2$ is an average dielectric permittivity and $\xi(\boldsymbol{r})$ is its deviation, so that $\langle \xi(\boldsymbol{r}) \rangle = 0$ (where angle brackets mean averaging), and p is the volume concentration of the grains.

The electric and magnetic fields can also be written as the sums of their average and fluctuation components, $\boldsymbol{E} = \boldsymbol{E} + \boldsymbol{e}, \boldsymbol{H} = \boldsymbol{H} + \boldsymbol{h}$. It has been proven that if different components of the fields fluctuate independently, then the usual expression for the Poynting vector holds for the average values:[78]

$$\langle \boldsymbol{S}\rangle = \frac{1}{8\pi}[\boldsymbol{E}(\boldsymbol{r})\times \boldsymbol{H}(\boldsymbol{r})]$$

The average electric field obeys the equation

$$\Delta \boldsymbol{E} + \frac{\omega^2}{c^2}(\varepsilon \boldsymbol{E} + \boldsymbol{\Pi}) = -\frac{1}{\varepsilon}\text{grad div}\boldsymbol{\Pi}, \text{ where}$$

$$\boldsymbol{\Pi}(\boldsymbol{r}) = \Pi_x(\boldsymbol{r}) = \vartheta^2 \boldsymbol{E}_x e^{ip_z z}\int \left[\frac{\omega^2}{c^2} - \frac{(k_z - p_z)^2}{\varepsilon}\right] \times \frac{\tilde{W}(\boldsymbol{p}-\boldsymbol{k})}{k^2 - \varepsilon\omega^2/c^2 - i0}\frac{d^3k}{(2\pi)^3} \quad (30)$$

In deriving Eq. (30), we have assumed propagation along the z-axis and an electric field polarization in the x-direction. In Eq. (30), $\vartheta^2 = \langle \xi^2\rangle = p(1-p)(\varepsilon_1 - \varepsilon_2)^2$, $\boldsymbol{E}_x$ is an amplitude of the electric field, p_z is the wave vector of light, and $\tilde{W}(k) = \int W(\rho)e^{-ip\rho}d^3\rho$ is the Fourier transform of the normalized correlation function $W(r) = \langle \xi(0)\xi(r)\rangle/\langle \xi^2\rangle$. It is evident from Eq. (30) that the real part of $\boldsymbol{\Pi}$ is the correction to the average permittivity ε, while its imaginary part corresponds to wave attenuation.

For a rough estimate, let us assume an expression for the correlation function $W(\rho)$:

$$W(\rho) = \exp(-\rho/R) \quad (31)$$

where R is the correlation length (this value is approximately comparable with the mean grain size). The exponential correlation function (31) is more suitable for a two-component grain structure than the commonly used Gauss function. Equation (31) assumes that the dielectric permittivity can be equal to ε_1 or ε_2, but not an intermediate value.[79,80] This is in agreement with Eq. (29). Note that the Fourier transform of (31) has a power decay factor with k, rather than an exponential one.

$$W(k) = \frac{8\pi R^3}{(1+k^2R^2)^2}$$

Assuming $(\omega/c)R \ll 1$ in Eq. (30), which means that the wavelength exceeds the grain size, we obtain an effective dielectric permittivity of

$$\tilde{\varepsilon} = \varepsilon - \frac{\vartheta^2}{3\varepsilon} + \frac{2}{3}i\vartheta^2\sqrt{\varepsilon}(\omega R/c)^3 \quad (32)$$

The correction factor is $p(1-p)(\varepsilon_1 - \varepsilon_2)^2/3\varepsilon$ for an effective permittivity with binary structure.[36] It is correct when dielectric constants are close ($\varepsilon_1 \approx \varepsilon_2$), or if one of the compound components prevails ($p \ll 1$ or $p \approx 1$). The imaginary correction to the permittivity means that the wave decay factor is

$$\gamma = \frac{\vartheta^2}{3}\left(\frac{\omega}{c}\right)^4 R^3$$

Thus, the scattering length of the photon is

$$l_{\text{small}}(\omega) = \gamma^{-1} = 3\vartheta^{-2}R^{-3}(\omega/c)^{-4} \quad (33)$$

in agreement with Rayleigh's law.

Using the above analysis, we can estimate scattering of waves in non-organized granular media when the grain size is significantly smaller than the light wavelength. It can also be applied to porous materials with small pore size.

9. PROPAGATION OF ELECTROMAGNETIC WAVES IN POROUS MATERIALS

In this section, we consider the propagation of waves in materials with long-scale irregularity, in particular pores where the average pore size is on the order of or larger than the mean wavelength.

Let $P(x)dx$ be the number of pores in the unit volume whose size is between x and $x+dx$. If all pores have the same diameter d, $P(x) = N\delta(x-d)$, where $N = 6p/(\pi d^3)$, and p is the porosity. To estimate the MFP, we assume a total cross-section of pores in a $1\times 1\times l$ parallelepiped to have value equal to unity. Therefore

$$\frac{\pi l}{4}\int_\lambda^\infty P(x)x^2dx = 1$$

where $l = l(\lambda)$ is the MFP of the photon. Thus,

$$l^{-1} = \frac{\pi}{4}\int_\lambda^\infty P(x)x^2dx \quad (34)$$

To relate $P(x)$ with the correlation function $W(r)$, introduced in Section 8, note that the number of pores whose size is less than $2r$ is $\int_0^{2r}P(x)dx$, and their total volume is $(\pi/6)\int_0^{2r}P(x)x^3dx$. This value should be related to $p(1-p)[1-W(2r)]$. Therefore,

$$1 - W(r) = \tfrac{\pi}{6p(1-p)}\int_0^r P(x)x^3dx, \quad \text{and}$$
$$P(r) = -\tfrac{6p(1-p)}{\pi r^3}\tfrac{\partial W(r)}{\partial r} \quad (35)$$

Hence

$$l^{-1}(\lambda) = -\frac{3p(1-p)}{2}\int_\lambda^\infty \frac{1}{x}\frac{\partial W(x)}{\partial x}dx \quad (36)$$

For rough estimation we can assume $W(x) = \exp(-x/d)$. Then

$$l^{-1} = \frac{3p(1-p)}{2d}\int_\lambda^\infty \frac{W(x)}{x}dx$$

In this approximation, the MFP of photons with wavelength much smaller than pore size is

$$l_{\text{large}} = \frac{2d}{3p(1-p)(\gamma + \ln\frac{d}{\lambda})} \quad (37)$$

where $\gamma \approx 0.5772$ is Euler's constant.

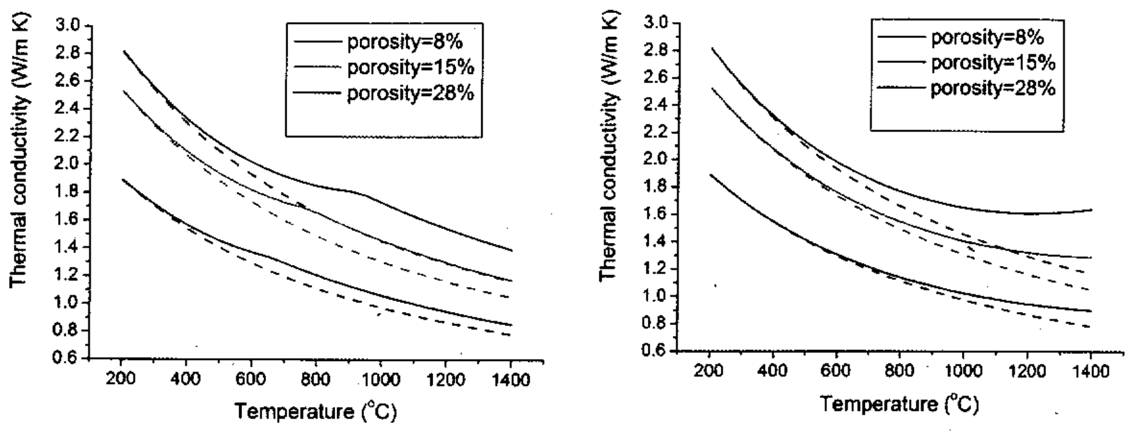

Fig. 48. Thermal conductivity of YSZ coatings with (solid lines) and without radiative component for coatings with small and large pores diameter (left: 0.5 μm, right: 100 μm).

Equations (36) and (37) yield estimates of the mean free path for the photons in materials with large-scale irregularity. Note that in the opposite limiting case $\lambda \gg R$, the integral in (36) results in an $l_{\text{large}} \sim \lambda \exp(\lambda/R)$. In this case, l_{large}^{-1} vanishes in Eq. (8).

A decrease in the porosity of YSZ yielding an increase of the radiative component of heat transfer is shown in Figure 48.

10. SIMULATION OF PHOTONIC STRUCTURES

The entire design of high-temperature photonic structures is a typical multiphysics problem because several disciplines of physics, such as electrodynamics, thermodynamics, and mechanics are simultaneously involved. Since differential equations may be used for describing the different physical aspects, one may essentially take advantage of very similar numerical methods that essentially integrate coupled differential equations based on one and the same numerical technique. Currently, several commercial multiphysics codes are available [http://www.comsol.com/], [http://www.cadfem.de/index.1810.0.html], [www.ansys.com/products/multiphysics.asp]. All of them are based on the Finite Elements Method (FEM).[82] There are several reasons for this. FEM is usually based on a tetrahedral, unstructured mesh that can easily be obtained from common CAD tools. All of the physical fields, such as the electrodynamic field components, temperatures, and stresses, can easily be approximated within a tetrahedral element by means of linear, quadratic or higher order functions. Therefore, once an FEM code is available, it is relatively easy to add modules for the different disciplines of physics. Finally, it is convenient for the users to work with the same methods for solving all of the problems involved.

However, when one focuses on the particular discipline of electromagnetics, FEM is neither the only available method nor the most efficient one, in general. Electromagnetics is a rather wide area, described by Maxwell's partial differential equations together with equations describing the material properties, the excitation of the electromagnetic field, and additional conditions such radiation conditions. Because of this, the efficiency of the numerical method depends strongly on the material properties and on the geometry properties of the structure to be analyzed. In particular, when non-linear materials are involved, time-domain techniques such as Finite Difference Time Domain (FDTD),[83] Finite Integral Technique in Time Domain (FIT-TD),[84] Finite Volume Time Domain (FVTD),[85] and FEM-TD[86] are best suited. Because of its simple implementation and fast iterative update schemes, FDTD is most frequently applied when non-linear materials are present. When material dispersion is strong, time domain methods become either expensive or inaccurate, and frequency domain methods are more favorable.

Although Finite Difference Frequency Domain (FDFD)[87] codes are available, these are not frequently applied. In the frequency domain, FEM and another class of codes based on boundary discretizations are most widely used. Boundary discretization means that only the boundaries between domains with different material properties need to be discretized. Thus, the dimension of the discretization space is reduced by one. As a result, boundary discretization methods lead to much smaller system matrices than domain discretization methods. On first sight, this leads to much smaller storage requirements and computation time, but the matrices of boundary discretization methods are dense while those of domain discretization methods are sparse. Whether a boundary discretization method is more efficient than a domain discretization method therefore depends on the specific implementation of the problem and its geometric details. When the geometry is relatively simple and may be defined analytically, one may derive and implement very powerful "semi-analytic" boundary discretization methods. These approaches usually suffer from a lack of generality, and may only be applied to certain problems.

Several techniques extend the semi-analytic approach to overcome these limitations. Most prominent among these are the Boundary Element Method (BEM)[88] and other methods based on Boundary Integral Equations (BIE),[89] the Generalized Multipole Technique (GMT),[90] with its Multiple Multipole Program (MMP),[91] the Method of Auxiliary Sources (MAS),[92] and the Method of Fictitious Sources (MFS).[93] All of these methods are general enough to handle arbitrary geometries, may provide highly accurate results, and exhibit very fast convergence—at least when the boundaries are smooth enough—but tend to become time consuming for complicated 3D problems. Therefore, boundary discretization methods are best suited when accurate results for simple 2D or axisymmetric 3D problems with dispersive, linear materials are desired, while domain discretization methods are better suited for obtaining not too accurate solutions of 3D problems with non-smooth geometry but dispersion-free materials.

Because of poor fabrication tolerances on the scale of nanometers, the limited accuracy of results obtained from domain discretization methods may seem to be of minor importance. This is not always true for the following reason. The optimal design of highly complex structures containing photonic crystals requires the detailed analysis of many different promising structures. Because of the complicated behavior of photonic crystals, simple design rules are often missing and the only reasonable way towards optimal solutions is to apply numerical optimizers.[94] Numerical optimizers usually "design" thousands of possible structures that must then be analyzed by an appropriate field solver, which finally calculates the quality or "fitness" of each structure and returns it to the optimizer. Numerical inaccuracies of the field solver cause some noise on the fitness function and can considerably disturb the optimizer.[95] As a result, the optimizer may run towards a sub-optimal solution or even towards an unrealistic solution that provides heavy numerical problems for the field solver. Thus designing by optimization demands an accurate field solver. When no highly accurate field solver is available for a certain problem type, the numerical optimizer must be designed in such a way that it is not too disturbed by noise on the fitness function. Such optimizers are more difficult to design and less efficient in general.

Because of the complexity of photonic structures, it is reasonable to design them within several steps. The first step is to analyze the band diagrams of hypothetically perfect photonic crystal structures that extend to infinity and are perfectly periodic. When total reflection is desired for a certain wavelength range, one must find a PhC structure with a band gap that includes the desired wavelength range. This is done by varying the crystal geometry and by appropriately selecting the materials that are used for constructing the photonic crystal. Currently, many powerful codes for obtaining the band diagrams are available. The most prominent one is based on the Plane Wave Expansion (PWE) method.[96]

In practice, photonic crystal structures must be finite. Thermal barrier coatings must consist of a finite number of photonic crystal layers perpendicular to the surface to be protected. Along the surface, the number of photonic crystal layers may be huge. Therefore, it is reasonable to study the impact of the finite number of layers by another model that still extends to infinity along the surface but is finite in the perpendicular direction as shown in Figure 5. This allows one to determine the required number of layers and to study the impact of fabrication tolerances. Consider the simple case of a Bragg-type photonic crystal coating with N layers consisting of two dielectrics D_1 and D_2 per layer. The structure is described by the two widths w_1 and w_2 of D_1 and D_2 that are equal for all N layers. Because of the fabrication tolerances, each width is disturbed by a few percent. As a result, one has a model with 2N geometric parameters $w_{11}, w_{21}, w_{12}, w_{22}, w_{13}, w_{23}, \ldots, w_{1N}, w_{2N}$. While this is tedious for the analysis of the impact of fabrication tolerances, it offers a way towards improved coatings: By an appropriate optimization of the 2D geometric parameters one may obtain a better performance. This optimization is very much similar to the optimization of anti-reflective coatings for optical lenses,[97] but with the opposite goal of maximizing reflection instead of minimizing reflection.

In order to illustrate the procedure, we consider a relatively simple cases of a five and ten layer dielectric slab system, such as ones studied previously.[98] In the case of HTPS, the materials are chose a priori in order to meet temperature requirements. For our example we will optimize a high-temperature, high-contrast Ti-SiO_2 structure. The optimizer chooses the thickness of each layer so as to minimize or maximize the reflection for a range of wavelengths. The most efficient and accurate solver for this problem is the analytic one. FDTD will also work well, but one must take care that fitness noise due to domain discretization does not limit the performance of the optimizer. This condition is satisfied when the FDTD results are similar enough to analytical ones to the degree that any error which arises from the discretization is less than the integration error encountered when evaluating the fitness from reflectance spectra. The benefit of the FDTD solution is that it is capable of tackling problems with complex geometries and materials.

Figure 49 shows results for the optimized five and ten layer systems. There are several resonances visible at higher frequencies, but their location is optimized so as to maximize the reflectance over a broad spectrum. Because of the addition degrees of freedom offered by the ten-layer system, the number of resonances increases, and better inter-resonance reflection is achieved. If we further restrict our optimization to a narrower band (between 1000 and 3000 nm), we can obtain even better in-band reflectance, at

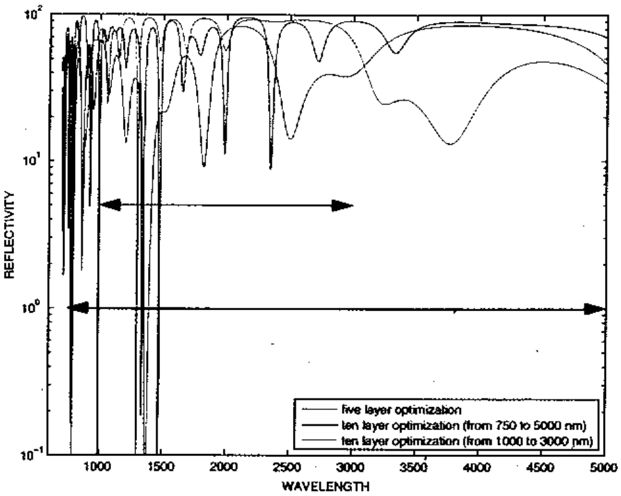

Fig. 49. Results of the FDTD optimization for the five and ten layer system. Here, it is demonstrated that the higher number of degrees of freedom which come with additional layers allows for an improvement of performance, while adding additional resonances to the reflectance behavior. By demanding less broadband performance, better higher in-band reflectance can be attained by the optimization.

the cost of reflectance outside the band. Consideration of the optimization fitness convergence curve for the narrowband optimization of Figure 49 shows that it is possible to obtain fast convergence for HTPS design when using efficient optimizers like the simple evolutionary strategy.[98]

11. CONCLUSIONS AND OUTLOOK

The search for newer, more efficient thermal barrier coatings is the focus of current HTPS studies. One dimensional high temperature photonic structures for ceramic thermal barrier coatings are studied most extensively. The application of metallo-dielectric metamaterials as IR sources, sensors, and spectral manipulators is one very promising direction. Many studies are devoted to surface structures for the control of spectral emissions from high-temperature materials. As a result of these studies, metal films with arrays of holes can be tuned to have band gaps at desired wavelengths. The dependence of thermal conductivity on photon mean free path is given. It was shown that long-range irregularities lead to a widening of the dip in transmittance spectra and increase the mid-gap transmittance of photonic structures. On the other hand, while short-range irregularities can increase the mid-gap transmittance, they do not cause a broadening of the dip. Equations for the scattering of electromagnetic radiation in non-organized granular materials are proposed. From both a theoretical and a technological points of view, porous high-temperature photonic structures appears to be the most realistic technique for fabricating durable thermally protective coatings. Design of HTPS is a typical multiphysics problem and can be handled using a number of finite element based techniques. When a precise consideration of wave propagation is required, the application of more sophisticated techniques is required. The design and optimization of photonic structures may be based on the analysis of the band diagram of a hypothetical structure possessing a desired photonic behavior over a desired wavelength range.

APPENDIX

Glossary of Acronyms Used

BEM	Boundary element method
BIE	Boundary integral equations
CMC	Ceramic matrix composite
CTE	Coefficient of thermal expansion
EB-PVD	Electron beam physical vapor deposition
FDFD	Finite difference frequency domain
FDTD	Finite difference time domain
FEM	Finite elements method
FEM-TD	Finite elements method in time domain
FFT	Fast fourier transformation
FIT-TD	Finite integral technique in time domain
FOD	Foreign object damage
FVTD	Finite volume time domain
GMT	Generalized multiple technique
HIP	High isostatic pressure
HTPS	High-temperature photonic structure
LWIR	Long wavelength infrared radiation
MAS	Method of auxiliary forces
MFP	Mean free path
MFS	Method of fictitious sources
MMP	Multiple multipole program
MWIR	Mid wavelength infrared radiation
ODC	Oxide defect cluster
ODR	Omnidirectional reflector
PBGM	Photonic band gap material
PBGM-DM	Photonic band gap material with density modulation
PBGM-RM	Photonic band gap material with refractive index modulation
PBGM-PM	Photonic band gap material with porosity modulation
PhC	Photonic crystal
PS	Plasma spray
PV	Photovoltaics
PWE	Plane wave expansion
RTC	Radiation thermal conductivity
SEBM	Selective electron beam melting
SEM	Scanning electron microscopy
TC	Thermal conductivity
TEBC	Thermal and environmental barrier coating
TEM	Transmission electron microscopy
TGO	Thermally grown oxide
TMM	Transfer matrix method
TPV	Thermophotovoltaics

UHC	Unburned hydrocarbons
YSZ	Yttria stabilized Zirconia (7YSZ means ZrO_2-7 wt% Y_2O_3)

References

1. J.-M. Lourtioz, H. Benisty, V. Berger, J.-M. Gerard, D. Maystre, and A. Tchelnokov, Photonic Crystals: Towards Nanoscale Photonic Devices, Berlin, Springer **(2005)**.
2. E. Yablonovitch, *Phys. Rev. Lett.* 58, 2059 **(1987)**.
3. S. John, *Phys. Rev. Lett.* 58, 2486 **(1987)**.
4. C. H. Seager, M. B. Sinclair, and J. G. Fleming, *Appl. Phys. Lett.* 86, 244105 **(2005)**.
5. H. Sai, H. Yugami, Y. Akiyama, Y. Kanamori, and K. Hane, *J. Opt. Soc. Amer. A* 18, 1471 **(2001)**.
6. M. J. Kelly, D. E. Wolfe, J. Singh, J. Eldridge, D.-M. Zhu, and R. Miller, *Int. J. Appl. Cer. Technol.* 3, 81 **(2006)**.
7. D. R. Clarke and C. G. Levi, *Annu. Rev. Mater. Res.* 33, 383 **(2003)**.
8. A. Polman and P. Wiltzius, *MRS Bulletin* 26, 608 **(2000)**.
9. D. Lusk and F. Placido, *Thin Solid Films* 492, 226 **(2005)**.
10. R. Siegel and C. M. Spuckler, *Mater. Sci. Eng. A* 245, 150 **(1998)**.
11. R. Koch, W. Krebs, and S. Wittig, *Proc. of International Symposium on Heat Transfer in the Turbomachinery*, edited by R. J. Goldstein, D. E. Metzger, and A. I. Leontiev, Begell House, Greece **(1994)**, p. 287.
12. D. Zhu and R. A. Miller, *Int. J. Appl. Ceram. Technol.* 1, 86 **(2004)**.
13. V. Sharma, J. Jiang, M. Hossu, A. R. Koymen, and S. Priya, *Appl. Phys. Lett.* 90, 123110 **(2007)**.
14. R. Vassen, N. Czech, W. Malléner, W. Stamm, and D. Stöver, *Surf. Coat. Technol.* 141, 135 **(2001)**.
15. D. Zhu and R. A. Miller, NASA/TM-2002-211481, May **(2002)**.
16. D. Zhu and Y. L. Chen, NASA/TM-2004-212480, January **(2004)**.
17. D. Zhu, Y. L. Chen, and R. A. Miller, NASA/TM-2005-213857, September **(2005)**.
18. Y.-C. Tsai, K. W.-K. Shung, and J. B. Pendry, *J. Phys.: Condens. Matter.* 10, 753 **(1998)**.
19. H. Ichi-oka, N. Higashi, Y. Yamada, T. Miyake, and T. Suzuki, *Diam. Rel. Mater.* 16, 1121 **(2007)**.
20. Z. L. Wang, R. P. Gao, J. L. Gole, and J. D. Stout, *Adv. Mater.* 12, 1938 **(2000)**.
21. C. Xu, Y. Zhan, K. Hong, and G. Wang, *Sol. St. Commun.* 10, 545 **(2003)**.
22. N. A. Bozkov and A. A. Ivanov, *J. Eng. Phys.* 541 **(1990)**. Translated from *Inzhenerno-Fizicheskii Zhurnal* 58, 714 **(1990)**.
23. W. P. J. Visser and S. C. A. Kluiters, NLR-TP-98629 **(1998)**.
24. A. G. Evans, D. R. Mumm, J. W. Hutchinson, G. H. Meier, and F. S. Petit, *Prog. Mater. Sci.* 46, 505 **(2001)**.
25. D. Zhu and R. A. Miller, NASA/TM-2004-213129, August **(2004)**.
26. I. Spitsberg and J. Steibel, *Int. J. Appl. Ceram. Technol.* 1, 291 **(2004)**.
27. L. P. Zawada, J. Staehler, and S. Steel, *J. Am. Ceram. Soc.* 86, 1282 **(2003)**.
28. L. Braginsky, V. Shklover, H. Hofmann, and P. Bowen, *Phys. Rev. B* 70, 134201 **(2004)**.
29. K. W. Schlichting, N. P. Padture, and P. G. Klemens, *J. Materials Science* 36, 3003 **(2001)**.
30. D. L. Wood and K. Nassau, *Applied Optics* 21, 2978 **(1982)**.
31. C. M. Cornelius and J. P. Dowling, *Phys. Rev. A* 59, 4736 **(1999)**.
32. S. John and J. Wang, *Phys. Rev. Lett.* 64, 2418 **(1990)**; *Phys. Rev. B* 43, 12772 **(1991)**.
33. F. O'Sullivan, I. Celanovic, N. Jovanovic, and J. Kassakian, *J. Appl. Phys.* 97, 033529 **(2005)**.
34. J. Singh, D. E. Wolfe, R. Miller, J. Eldridge, and D.-M. Zhu, *Mater. Sci. Forum* 455–456, 579 **(2004)**.
35. D. E. Wolfe, J. Singh, R. A. Miller, J. I. Eldridge, and D.-M. Zhu, *Surf. Coat. Techn.* 190, 132 **(2005)**.
36. L. D. Landau and E. M. Lifshitz, Electrodynamics of Continuous Media, Pergamon Press, Oxford **(1984)**.
37. S. Weiss, H. Ouyang, J. Zhang, and P. Fauchet, *Optics Express* 13, 1090 **(2005)**.
38. Y. Li, P. Kim, and M. Sailor, *Physica Status Solidi A* 202, 1616 **(2005)**.
39. M. Qian, X. Q. Bao, L. W. Wang, X. Lu, J. Shao, and X. S. Chen, *J. Cr. Growth* 292, 347 **(2006)**.
40. G. Witz, V. Shklover, W. Steurer, S. Bachegowda, and H.-P. Bossmann, *J. Amer. Cer. Soc.* 90, 2935 **(2007)**.
41. L. Braginsky and V. Shklover, *Phys. Rev. B* 73, 085107 **(2006)**.
42. O. Painter, K. Srinivasan, and P. E. Barclay, *Phys. Rev. B* 68, 035214 **(2003)**.
43. K. Busch, S. Mingaleev, A. Garcia-Martin, M. Schillinger, and D. Hermann, *J. Phys.: Condens. Matter* 15, R1233 **(2003)**.
44. E. Istrate, M. Charbonneau-Lefort, and E. H. Sargent, *Phys. Rev. B* 66, 075121 **(2002)**.
45. M. Charbonneau-Lefort, E. Istrate, M. Allard, J. Poon, and E. H. Sargent, *Phys. Rev. B* 65, 125318 **(2002)**.
46. J. P. Albert, C. Jouanin, D. Cassagne, and D. Bertho, *Phys. Rev. B* 61, 4381 **(2000)**.
47. R. B. Wehrspohn and J. Schilling, *MRS Bulletin* 26, 623 **(2001)**.
48. H. Masuda, H. Asoh, M. Watanabe, K. Nishio, M. Nakao, and T. Tamamura, *Adv. Mater.* 13, 189 **(2001)**.
49. A. P. Li, F. Müller, and U. Gösele, *Electrochem. Sol.-St. Letters* 3, 131 **(2000)**.
50. S. H. G. Teo, A. Q. Liu, J. Singh, M. B. Yu, and G. Q. Lo, *Appl. Phys. A* 89, 417 **(2007)**.
51. S. Assefa, P. T. Rakich, P. Bienstamn, S. G. Johnson, G. S. Petrich, J. D. Joannopoupus, L. A. Koldziejski, E. P. Ippen, and H. I. Smith, *Appl. Phys. Lett.* 85, 6110 **(2004)**.
52. W. Kuang, Z. Hou, Y. Liu, and H. Li, *J. Opt. A: Pure Appl. Opt.* 7, 525 **(2005)**.
53. Y. Yamamoto, J.-K. Chung, T. Sekino, T. Kusunose, T. Nakayama, C.-J. Kim, and K. Niihara, *J. All. Comp.* 385, 252 **(2004)**.
54. J.-J. Greffet, R. Carminati, K. Joulain, J. P. Mulet, S. Mainguy, and Y. Chen, *Nature* 416, 61 **(2002)**.
55. J. G. Fleming, S. Y. Lin, I. El-Kady, R. Biswas, and K. M. Ho, *Nature* 417, 52 **(2002)**.
56. M. M. Sigalas, C. T. Chan, K. M. Ho, C. M. Soulokous, *Phys. Rev. B* 52, 11744 **(1995)**.
57. M. U. Pralle, N. Moelders, M. P. McNeal, I. Puscasu, A. C. Greenwald, T. George, D. S. Choi, I. El-Kady, and R. Biswas, *Appl. Phys. Lett.* 81, 4685 **(2002)**.
58. E. Wolf, *Nature* 326, 363 **(1987)**.
59. E. Wolf and D. F. James, *Rep. Prog. Phys.* 59, 771 **(1996)**.
60. I. Puscasu, M. Pralle, M. McNeal, J. Daly, A. Greenwald, E. Johnson, R. Biswas, and C. G. Ding, *J. Appl. Phys.* 98, 013531 **(2005)**.
61. R. Biswas, C. G. Ding, I. Uscasu, M. Pralle, M. McNeal, J. Daly, A. Greenwald, and E. Johnson, *Phys. Rev. B* 74, 045107 **(2006)**.
62. S.-Y. Lin, J. G. Fleming, E. Chow, J. Bur, K. K. Choi, and A. Goldberg, *Phys. Rev. B* 62, R2243 **(2000)**.
63. I. El-Kady, W. W. Chow, and J. G. Fleming, *Phys. Rev. B* 72, 195110 **(2005)**.
64. J. M. Gee, S. Lin, J. G. Fleming, and J. B. Moreno, US Patent No. 6'611'085-B1, August **(2003)**.
65. S. Y. Lin, J. Moreno, and J. G. Fleming, *Appl. Phys. Lett.* 83, 380 **(2003)**.
66. S. Y. Lin, J. Moreno, and J. G. Fleming, *Appl. Phys. Lett.* 84, 1999 **(2004)**.
67. J. G. Fleming, *Appl. Phys. Lett.* 86, 249902 **(2005)**.
68. S.-Y. Lin, J. G. Fleming, and I. El-Kady, *Appl. Phys. Lett.* 83, 593 **(2003)**.
69. J. G. Fleming, S. Y. Lin, I. El-Kady, R. Biswas, and K. M. Ho, *Nature* 417, 52 **(2002)**.

70. C. Viney, *Curr. Opinion in Sol. St. Mater. Sci.* 8, 93 (**2004**).

71. M. K. Alam, S. Tkach, and S. L. Semyatin, *Exp. Heat Transfer* 13, 39 (**2000**).

72. Y.-C. Tsai, K. W.-K. Shung, and J. B. Pendry, *J. Phys. Cond. Matt.* 10, 753 (**1998**).

73. K. E. Perepelkin, *Khimicheskie Volokna* 4, 27 (**1991**).

74. V. N. Astratov, A. M. Adawi, S. Fricker, M. S. Skolnick, D. M. Whittaker, and P. N. Pusey, *Phys. Rev. B* 66, 165215 (**2002**).

75. V. Shklover, L. Braginsky, and H. Hofmann, *Mat. Sci. Eng. C* 70, 142 (**2006**).

76. Yu. A. Vlasov, M. A. Kaliteevski, and V. V. Nikolaev, *Phys. Rev. B* 60, 1555 (**1999**).

77. L. Braginsky and V. Shklover, *Phys. Rev. B* 73, 085107 (**2006**).

78. L. Braginsky, V. Shklover, H. Hofmann, and P. Bowen, *Phys. Rev. B* 70, 134201 (**2004**).

79. M. V. Berry, *Philis. Trans. R. Soc. London, Ser. A* 273, 611 (**1973**).

80. J. M. Ziman, Models of Disorder. The Theoretical Physics of Homogeneously Disordered Systems, Cambridge University Press, Cambridge (**1979**), p. 79.

81. L. Braginsky, V. Shklover, G. Witz, and H.-P. Bossmann, *Physical Review B* 75, 094301 (**2007**).

82. J. L. Volakis, A. Chatterjee, and L. C. Kempel, Finite Element Method Electromagnetics: Antennas, Microwave Circuits, and Scattering Applications, Wiley-IEEE Press, New York (**1998**).

83. A. Taflove, The Finite-Difference Time-Domain Method, Artech House, Norwood, MA (**1995**).

84. T. Weiland, *Electronics and Communications AEU* 31, 116 (**1977**).

85. P. Bonnet, X. Ferrieres, and F. Isaac, *Waves and Applications* 11, 1189 (**1997**).

86. A. Bertolani, A. Cucinotta, S. Selleri, L. Vincetti, and M. Zoboli, *Optical and Quantum Electronics* 35, 1005 (**2003**).

87. C.-P. Yu and H.-C. Chang, *Opt. Express* 12, 1397 (**2004**).

88. F. Leydecker, hp-version of the boundary element method for electromagnetic problems, thesis University of Hannover (**2006**), http://deposit.ddb.de/cgi-bin/dokserv?idn=982597819.

89. Y.-W. Kiang, J.-Y. Wang, and C. C. Yang, *Opt. Express* 15, 9048 (**2007**).

90. Ch. Hafner, The Generalized Multipole Technique for Computational Electromagnetics, Artech House, Boston (**1990**).

91. Ch. Hafner, Post-Modern Electromagnetics Using Intelligent MaXwell Solvers, John Wiley & Sons, New York, Chichester, Brisbane, Toronto (**1999**).

92. F. G. Bogdanov, D. D. Karkashadze, and R. S. Zaridze, Generalized Multipole Techniques for Electromagnetic and Light Scattering, edited by T. Wriedt, Elsevier, Amsterdam (**1999**), pp. 143–172.

93. D. Maystre, M. Saillard, and G. Tayeb, Special Methods of Wave Diffraction in Scattering, edited by P. Sabatier and E. R. Pike, Academic Press, London (**2001**).

94. Ch. Hafner, J. Smajic, and D. Erni, Simulation and optimization of composite doped metamaterials, Handbook of Theoretical and Computational Nanotechnology, American Scientific Publishers, California (**2005**).

95. Ch. Hafner, C. Xudong, J. Smajic, and R. Vahldieck, *J. Opt. Soc. Am. A* 24, 1177 (**2007**).

96. S. G. Johnson and J. D. Joannopoulos, Photonic Crystals: The Road from Theory to Practice, Kluwer Academic Publishers, Boston, MA (**2002**).

97. M. Mishrikey, A. Fallahi, C. Hafner, and R. Vahldieck, *International Symposium on Optomechatronic Technologies*, Lausanne, October (**2007**).

98. H.-G. Beyer and H.-P. Schwefel, *Journal Natural Computing* 1, 52 (**2002**).

99. I. H. Malitson, *J. Opt. Soc. Amer.* 52, 1377 (**1962**).

100. I. H. Malitson, *J. Opt. Soc. Amer.* 55, 1205 (**1965**).

101. Y. Nigara, *Jpn. J. Appl. Phys.* 7, 404 (**1968**).

102. D. L. Wood and K. Nassau, *Appl. Opt.* 21, 2978 (**1982**).

103. R. E. Stephens and I. H. Malitson, *J. Res. Nat. Bur. Stand.* 49, 249 (**1952**).

104. G. B. Scott, D. E. Lacklison, and J. L. Page, *Phys. Rev. B* 10, 971 (**1974**).

105. N. P. Padture and P. G. Klemens, *J. Am. Cer. Soc.* 80, 1018 (**1997**).

106. O. Medenbach and R. D. Shannon, *J. Opt. Soc. Am. B* 14, 3299 (**1997**).

107. R. D. Shannon, R. C. Shannon, O. Medenbach, and R. X. Fischer, *J. Phys. Chem. Ref. Data* 31, 931 (**2002**).

108. X. Q. Cao, R. Vassen, and D. Stoever, *J. Eur. Cer. Soc.* 24, 1 (**2004**).

109. M. A. Ordal, L. L. Long, R. J. Bell, R. R. Bell, R. W. Alexander, Jr., and C. A. Ward, *Appl. Opt.* 22, 1099 (**1983**).

110. S. Adachi, *Phys. Rev. B* 38, 12966 (**1988**).

111. P. B. Johnson and R. W. Christy, *Phys. Rev. B* 9, 5056 (**1974**).

112. B. J. Stagg and T. T. Charalampopoulos, *Combustion and Flame* 94, 381 (**1993**).

Received: 10 October 2007. Accepted: 22 October 2007.